Computer Modeling in Engineering & Sciences

Tech Science Press

https://doi.org/10.32604/cmes.2026.077616

ARTICLE

AI-Assisted Hybrid Solver for Skin Friction and Sherwood Number Prediction in Eyring–Prandtl Nanofluid Flow over a Riga Plate

Yasir Nawaz[1], Nabil Kerdid[2], Muhammad Shoaib Arif[3] and Mairaj Bibi[4,*]

[1]Department of Mathematics, Faculty of Engineering and Computing, National University of Modern Languages (NUML), Islamabad, Pakistan

[2]Department of Mathematics and Statistics, College of Science, Imam Mohammad Ibn Saud Islamic University (IMSIU), Riyadh, Saudi Arabia

[3]Department of Mathematics and Sciences, College of Sciences and Humanities, Prince Sultan University, Riyadh, Saudi Arabia

[4]Department of Mathematics, COMSATS University Islamabad, Park Road, Islamabad, Pakistan

*Corresponding Author: Mairaj Bibi. Email: mairaj_maths@comsats.edu.pk

Received: 13 December 2025; Accepted: 26 January 2026; Published: 26 February 2026

ABSTRACT: A high-order hybrid numerical framework is developed by coupling a three-stage exponential time integrator with a Runge–Kutta scheme for the efficient solution of partial differential equations involving first-order time derivatives. The proposed scheme attains third-order temporal accuracy and is rigorously validated through stability and convergence analyses for both scalar and coupled systems. Its effectiveness is demonstrated by simulating unsteady Eyring-Prandtl non-Newtonian nanofluid flow over a Riga plate with coupled heat and mass transfer under electromagnetic actuation. The physical model accounts for Brownian motion and thermophoresis, and the nanofluid considered is a Prandtl-type non-Newtonian base fluid containing suspended nanoparticles, with heat and mass transport governed by coupled momentum, energy, and concentration equations. Numerical simulations are performed over practically relevant parameter ranges, with the Reynolds number fixed at $Re = 5$ and the Prandtl number set to $Pr = 3$ to represent moderate inertial and thermal diffusion effects typical of nanofluid transport systems. To enhance computational efficiency, an artificial neural network (ANN)-based surrogate model is developed to predict the skin friction coefficient and local Sherwood number as functions of Reynolds number, Prandtl number, Schmidt number, Brownian motion, and thermophoresis parameters. The training dataset is generated entirely from high-fidelity numerical simulations produced by the proposed hybrid scheme. The data are systematically partitioned into 70% for training, 15% for validation, and 15% for testing, ensuring reliable generalization. Regression analysis yields a near-unity correlation coefficient ($R \approx 0.99$), while error histograms exhibit tightly clustered residuals around zero, confirming high predictive accuracy. Furthermore, a benchmark convergence study using Stokes' first problem demonstrates that the proposed scheme consistently achieves lower global error norms than the classical Runge–Kutta method for identical spatial and temporal resolutions. Overall, this study introduces a novel computational intelligence framework that integrates high-order numerical solvers with machine learning, offering a robust and time-efficient tool for advanced modeling and real-time prediction of non-Newtonian nanofluid transport phenomena under electromagnetic flow control.

KEYWORDS: Eyring-Prandtl nanofluid; Riga plate; heat and mass transfer; hybrid numerical scheme; neural network prediction

1 Introduction

Non-Newtonian fluids play a central role in modern industrial, biomedical, and energy-related applications due to their complex rheological behaviour that cannot be modelled using classical Newtonian assumptions. Such fluids arise naturally in polymer melts, drilling muds, biofluids, paints, lubricants, and slurry transport systems. Among the many constitutive models proposed to describe non-Newtonian behaviour, the Eyring–Prandtl fluid model is recognized for its ability to capture shear-thinning effects arising from molecular activation-energy mechanisms. The Eyring-Prandtl formulation is an attractive choice for high-accuracy transport modelling, unlike power-law or Bingham models, because it can yield a physically realistic stress-strain relationship over a wide range of shear rates.

However, over the last few years, nanoparticles incorporated into base fluids to create nanofluids have attracted considerable interest due to their high heat and mass transfer rates. The nanoparticles increase thermal conductivity, diffusive transport, and chemical reactivity, which are essential in applications such as heat exchangers, cooling of electronic devices, chemical reactors, biomedical drug delivery, and solar energy systems. The joint play of non-Newtonian rheology and nanoparticle transport processes, specifically Brownian motion and Thermophoresis, results in highly non-linear transport behaviour, which requires sophisticated computational treatment.

One reason nanofluid flow is of interest is its interaction with electromagnetic actuation, where Lorentz forces can significantly affect the momentum boundary layers. In this regard, the Riga plate, initially proposed by Gailitis et al. [1], has proven to be a viable electromagnetic actuator for manipulating the boundary layer. The plate consists of periodically spaced permanent magnets and electrodes beneath the surface, which generate a Lorentz force parallel to the wall that can accelerate or decelerate the fluid layers near the wall, depending on the applied electrical conditions. The unmatched mechanism contributes to the plate of Riga, making it very efficient at reducing drag forces, stabilizing fluids in high-temperature systems, eliminating heat in high-temperature systems, micro-pumping, and improving mixing in microreactors. In turn, the study of the Eyring-Prandtl nanofluid flow over a Riga plate provides valuable insights into the underlying transport processes and design-oriented approaches for present-day electromechanical systems.

Choi [2] first used the phrase “nano liquid” to describe a solution containing nanoparticles suspended in a conventional fluid, such as water, oil, or ethylene glycol. In applications involving heat transfer, such as microprocessors, energy engines, hybrids, and temperature reduction, nanomaterials play an essential role. Two additional elements, Brownian motion and thermophoretic force, were added to Buongiorno’s [3] mathematical formulation. Then, via a thermal mechanism between two surfaces, Islam et al. [4] discussed the MHD flow of micropolar nanofluids. To understand how a nano liquid behaves, Alempour et al. [5] described an elliptical cross-section of tubes with spinning walls. Rasool et al. [6] analyzed the entropy of the nanoliquid’s Darcy-Forchheimer flow past the non-linear sheet. Tanveer and Malik [7] conducted numerical studies on the slip impact of a Ree-Eyring nanofluid in peristaltic flow across a curved surface. For instance, Khan et al. [8] investigated the influence of the Lorentz force on Ree–Eyring nanomaterial flow over a paraboloid stretching surface. They demonstrated that magnetic effects can effectively modulate velocity and thermal boundary layers. Nano-liquid flow has been extensively studied, with heat transfer and thermal conductivity as defining characteristics [9–13]. Mkhatshwa et al. [14] addressed the Hall effect and the effect of a chemical reaction on the physical properties of a hybrid nanofluid. An explanation of the three-dimensional Darcy-Forchheimer flow of an Eyring-Powell nanoliquid through a porous medium was provided by Tlili et al. [15]. Thermodynamic slip in Oldroyd-B fluid magnetized axi-symmetric flow with infinite stretchable disks was investigated by Khan et al. [16].

Over the last several decades, the inherent value of porous media has been recognized in an increasing number of important sectors. Porous media enhance nanoparticle scattering and increase the success rate

by increasing the contact area between a fluid and a strong surface. Consequently, the effectiveness of conventional thermal frameworks is greatly enhanced [17]. When the flow rate is low (Reynolds number < 1), Darcy's law applies to flow through porous media. Even though Darcy's law accurately describes most streams in porous media, it breaks down at high flow rates. Forchheimer correlations point to higher flow rates. The Forchheimer term, an additional non-linear velocity term, was first developed by Forchheimer [18].

At large Reynolds numbers, it was also described as a huge "Forchheimer term" by Muskat [19]. For example, Seddeek [20] looked at how viscous dissipation and thermophoresis affect a system, Francis et al. [21] looked at the Cattaneo-Christov heat transition model, Arulmozhi et al. [22] looked at how heat and mass transfer behave in MHD nanofluid flow over an infinite moving vertical plate under combined radiative and chemical reactive effects, Hayat et al. [23] looked at what happens when thermal conductivity changes, and every article that dealt with Darcy-Forchheimer flow was systematically searched. Using the Darcy-Forchheimer porous media model, Mohana and Kumar [24] successfully simulated three-dimensional hybrid nanofluid flow over a stretched sheet, incorporating form drag and convective heat transfer. In their study, Animasaun et al. [25] recorded the Darcy flow of a ternary-hybrid nanofluid. Prakash et al. [26] computed a Darcy-Forchheimer porous medium for an Electro-magneto-hydrodynamic (EMHD) ternary hybrid non-Newtonian nanofluid using zeta potential and wall suction/injection effects across a wedge.

Applying opposing electric and magnetic fields never results in a uniformly directed flow. A paradoxical electric current, the Hall current, flows through an electric field that is perpendicular to a magnetic field in the Hall effect [27]. One possible explanation is the Hall current, which is amplified by the strong magnetic field. When a fluid with electrical conductivity moves across a magnetic field, a phenomenon known as a transverse flow happens. This flow defies Ohm's law. The Hall effect resolves several proven issues and makes it easier to identify various flow parameters in a flow field. Hall current's effects on the maximum hydrodynamic drag (MHD) flow of a thick, non-compressible, electrically conducting fluid are of considerable theoretical and practical interest to scientists because of the many practical and theoretical uses for this phenomenon [28]. A few examples of the many applications of Hall current include flow-through filtering devices, thermal energy storage, Hall monitors, Hall accelerators, rotors, and MHD power sources [29]. Several devices rely on biomechanics and mechanics, such as biomicro pumps, bioreactors for membrane oxygenators, biochips, and magnetic resonance angiography (MRA) [30]. A nanofluid in a combined cone-and-disk geometry is analyzed using Hall currents, following the example by Basavarajappa and Bhatta [31]. Recent studies have explored heat and mass transfer in non-Newtonian Casson nanofluids over wedge-shaped stretching surfaces using advanced numerical techniques, highlighting the influence of nonlinear stretching and unsteady flow on transport characteristics [32]. Entropy generation and boundary layer behavior in Casson nanofluids have also been investigated under nonlinear and unsteady conditions, providing valuable benchmarks for modeling complex nanofluid systems [33].

Oil pipeline friction, central heating and refrigeration applications, enhanced capacity, and flow tracers are just a few examples of the many industrial, biological, chemical, and technological domains that make the transport and flow processes of non-Newtonian fluids fascinating to researchers and scientists [34]. Non-Newtonian materials have become more common in industrial sectors over the last few decades, while Newtonian materials have remained prevalent. Reason being, when compared to Newtonian fluids, non-Newtonian fluids are better at predicting elastic properties because of their higher viscoelastic qualities [35]. It is also widely recognized that most fluids in the body do not behave as Newtonian fluids. Some fluids that do not adhere to Newton's rule of viscosity are actually viscoelastic due to their inherent properties [36]. It means that when shear tension is low, flow is absent. So, for fluids that aren't Newtonian, yield stress is the sole stress. The list of non-Newtonian fluids includes things like concentrated juices, pulp, jellies, paints, sugar solutions, clay films, concentrated juices again, honey, drilling pozzolans, synthetic lubricants, speciality oils, and blood.

A novel technology with enormous energy-saving potential, expandable consumption might be included in district heating and cooling systems, as well as building Heating, Ventilation, and Air Conditioning (HVAC) systems. Incorporating a colour scheme with non-Newtonian features yielded a highly effective flow tracker. To prevent dispersion and breakdown, they are used to create a tracer fluid. This fluid is subsequently introduced into a turbulent flow as a thin strip. The simple Navier-Stokes equations cannot sufficiently describe the flow field properties of non-Newtonian fluids because the mathematical formulation required to model the flow problem is complex. Through a penetrating exponentially vertical cone, Gomathi and Poulomi [37] explored the potential for optimizing the entropy of an EMHD Casson-Williamson penta-hybrid nanofluid.

A further level of complexity emerges when nanofluid flow is exposed to electromagnetic actuation, particularly in the presence of a Riga plate. Specialized electromagnetic surfaces include the Riga plate, which consists of alternating layers of permanent magnets and electrodes that generate a spatially varying Lorentz force parallel to the plate surface. This externally manageable force allows near-wall flow dynamics to be directly controlled, thereby enabling the effective manipulation of boundary layers, frictional resistance, and heat/mass transport rates. Riga plate configurations have been highly beneficial for drag reduction, flow stabilization, microfluidic pumping, thermal control at high temperatures, and nanocoating technologies. Therefore, the research on the Eyring-Prandtl nanofluid flow past a Riga plate is an essential contribution to both Theory and practical engineering of thermal mass transport.

The correct determination of the skin friction coefficient and the local Sherwood number is paramount for engineering. The skin friction coefficient measures surface drag and energy loss, and the Sherwood number measures the efficiency of mass transfer at the solid-fluid interface. Such amounts are fundamental to streamlining surface coating, separation technologies, biomedical mass diffusion, and catalytic surface reactions. However, under the combined effects of non-Newtonian rheology, MHD forces, nanoparticle diffusion, and electromagnetic control, the resulting governing equations become strongly non-linear and tightly coupled, rendering closed-form analytical solutions impractical.

Nanofluids are manufactured fluids made by dispersing nanoparticles into more traditional base fluids. These particles can be anything from metals and metal oxides to carbides and carbon nanotubes. Because of their improved thermophysical properties, these suspensions work wonders for increasing thermal conductivity. Nanofluids have many potential uses across industries, including hybrid power systems, home refrigeration, thermal management in electronics, medicinal procedures, and high-performance heat exchangers. Currently, three main coupling models are available. The first model, starting with the data-driven paradigm, allows the input-output link to be derived without any physical mechanisms. After that, the physical framework model uses AI algorithms to improve the previous models. The tertiary model combines physical processes with data-driven ones. While there are numerous AI algorithms available, data-driven models are where the ANN really shines. Aerodynamic modeling, turbulence modeling, specialized flows, and mass and heat transport phenomena are five areas where it has been effectively used. Physical model scenarios typically employ several other AI approaches, including recurrent neural networks (RNNs), naïve Bayes (NB) algorithms, and support vector machines (SVMs).

Recent studies indicate that machine learning models are being applied to estimate fluid thermophysical properties and to explore correlations between the skin friction, the Nusselt number, and other fluid mechanics variables. We look at some of the research. Shafiq et al. [38] first attempted to estimate the skin friction coefficient and Nusselt number using artificial neural networks (ANNs). In their analysis of the temperature-Biot number correlation, they found that ANN was the best solution. The Sherwood, Nusselt, and skin-friction coefficients have been approximated using an ANN model for non-Newtonian fluids over

two spinning disks, as done by Zhao et al. [39]. A Darcy-Forchheimer mixed nanofluid flow in a revolving Riga disk was studied by Sharma et al. [40].

The prediction of hybrid nanofluid properties also uses an ANN in conjunction with the Levenberg-Marquardt backpropagation method. Predicting fluid properties was one of the ANN's identified uses. Similarly, Boumari et al. [41] used ANNs and the Levenberg-Marquardt algorithm to investigate heat transfer through helical tubes and to calculate the Nusselt number. Two parameters were input to the model: the nanoparticle volume percentage and the Reynolds number. The exergy efficiency, frictional entropy, and heat entropy production of $CoFe_2O_4$/Water nanofluids were studied by Sundar and Mewada [42] using ANFIS and multilayer perceptrons as well. The impact of a spinning cylinder on the phase behavior variation in an L-shaped ventilation chamber was modelled by Ouri et al. [43] using an ANFIS-based model. When investigating the nanofluid Sherwood numbers in turbulent flows, Beiki [44] found that ANFIS was quite helpful, and when researching laminar flows, FCM-ANFIS was even more so.

Inspired by the structure and function of the real brain, artificial neural networks are computational representations of interconnected networks of neurons. To create forecasts using data patterns, explicit programming is superfluous. Predicting flows, simulating turbulence, estimating properties, enhancing systems, and controlling flows are all examples of fluid mechanics in action. Artificial neural networks (ANNs) aid these endeavours by developing turbulence models, accurately predicting flow behaviour, and optimizing system efficiency. Using ANN systems in conjunction with genetic algorithms, Ahmadi et al. [45] calculated pressure reductions in automotive radiators containing nanofluids. Using ANN modeling and multi-objective optimization, Hojjat [46] investigated nanofluids as coolants in shell-and-tube heat exchanger topologies. The Darcy-Forchheimer Ree-Eyring fluid flow with an activation energy and a convective boundary condition, as it pertains to a porous stretched layer, can be effectively simulated using an ANN, according to studies done by Shafiq et al. [47]. The constructed ANN is a practical engineering method that, as stated in [48], may deliver extremely accurate forecasts and can be used in reliability analysis via the inverse power law with Bayesian regularization. By incorporating nanofluid properties into their ANN-imitated microchannel heat exchanger model, Kamsuwan et al. [49] improved the simulation. To accurately anticipate heat transfer rates, fluctuations in the Nusselt number, and entropy generation, Habib et al. [50] created an ANN framework for heat and mass transfer through a porous Riga surface. The recent work [51], which uses a soft computing-based approach to enhance heat transfer in reactive nanofluid flows, aligns well with our focus on AI-assisted modeling of non-Newtonian flows with thermal mass transport mechanisms.

Moreover, simultaneous forecasting of the local Sherwood number and the skin friction coefficient is instrumental for describing the behaviour of surface drag and mass transfer. The parameters are fundamental for optimizing industrial equipment such as heat exchangers, nanocoating processes, separation equipment, biomedical sprays, and chemical reactors. Conventional analysis techniques fail to provide nonlinearities in coupled magnetohydrodynamic (MHD) forces, nanoparticle diffusion, and non-Newtonian rheology. Hence, to study such multi-physics interactions, numerical simulation is the best method of analysis. Yet numerical solvers are computationally intensive, particularly when parameter sweeps or optimization studies are required.

More recent studies have suggested moving beyond these constraints by adopting hybrid computational strategies that combine physics-based numerical workflows with machine learning (ML) and neural network (NN) models. Neural networks are beneficial for non-linear computations of flow parameters into engineering quantities of interest and can be trained quickly to provide rapid surrogate forecasts. NN-based models have been effectively used in fluid mechanics and heat transfer for predicting drag and thermal conductivity, and for predicting nanoparticle concentration and optimizing in complex geometries.

Although these achievements have been made, their combination with non-linear and non-Newtonian nanofluid flows in the presence of electromagnetic surfaces, e.g., Riga plates, has been only briefly explored.

Consequently, high-accuracy numerical schemes have become essential for simulating such complex transport processes. Explicit and implicit Runge-Kutta methods, finite difference methods, and predictor-corrector methods, which are commonly used as classical time-integration methods, can be either unstable, inaccurate, or simply too expensive to solve stiff magnetohydrodynamic nanofluid systems. Exponential integrators are newer alternatives that have been effective in addressing these limitations in solving time-dependent partial differential equations because they are more stable and better at handling stiffness. However, even isolated exponential approaches can be inaccurate in solving non-linear source equations.

Both of these observations lead to the present work, which suggests a hybrid numerical scheme built based on an exponential integrator and a Runge-Kutta method. The obtained scheme is 3rd-order accurate, has three computational steps, and is designed to effectively handle first-order time-dependent non-linear partial differential equations governing the temporal dynamics of nanofluid transport. The stability and convergence behaviour of both scalar equations and coupled Partial differential equation (PDE) systems are rigorously analyzed, and the method is strongly mathematically reliable. It is followed by the application of the proposed scheme to simulate Eyring-Prandtl nanofluid flow over a Riga plate, accounting for coupled heat and mass transfer, thereby enabling the accurate calculation of velocity, concentration, the skin friction coefficient, and the Sherwood number profile.

Although the solutions to numerical simulations are high-fidelity, repeated simulations across a broad parameter space (Reynolds number, Prandtl number, Schmidt number, thermophoresis parameter, and Brownian motion parameter) may entail high computational costs. To address this challenge, the current study further incorporates artificial intelligence-based prediction using a neural network model. Recently, neural networks have been shown to possess an impressive ability to learn non-linear mappings between physical inputs and engineering outputs in the study of fluid mechanics, heat transfer, and transport modelling. Such models can make instant predictions with very little computational effort after training and are therefore ideal for real-time optimization and control.

Novelty of this study: In this work, a numerically generated dataset is used to train a neural network capable of predicting the skin friction coefficient and the local Sherwood number with high accuracy. To validate the neural model's learning performance, error histograms and regression plots of predicted outputs vs. target data are presented, confirming the robustness and reliability of the AI-based predictor. This hybrid numerical–neural framework thus combines the physical interpretability of numerical simulation with the computational efficiency of artificial intelligence.

Finally, the performance of the proposed hybrid numerical scheme is assessed through a comparative analysis with an existing numerical method, demonstrating that the present scheme produces significantly lower numerical error for selected step sizes. This confirms both the efficiency and accuracy advantages of the developed approach. Here are the main points of this work's contributions:

1. We developed a third-order-accurate, three-stage hybrid exponential–Runge–Kutta numerical scheme for non-linear time-dependent PDEs.
2. We provided a rigorous stability and convergence analysis for both scalar and coupled PDE systems.
3. We developed mathematical models and numerical simulations of Eyring–Prandtl nanofluid flow over a Riga plate with heat and mass transfer.
4. Accurate computation and AI-based prediction of skin friction coefficient and local Sherwood number.
5. A comparative analysis demonstrates that the neural predictor achieves high accuracy while significantly reducing computational cost compared to repeated simulations.

6. The combined framework serves as a promising hybrid modelling tool for real-time optimization of nanofluid-based thermal and mass transfer systems.

This study offers a novel collaboration between computational fluid dynamics and artificial intelligence to improve predictive capability and reduce computational burden in modelling complex non-Newtonian nanofluid flows. The results highlight the practical potential of hybrid models for advancing the design of next-generation engineering devices that involve MHD actuation and nanoscale transport processes.

In the remainder of this study, Section 2 describes the construction of the proposed hybrid numerical scheme, combining a modified exponential integrator with the classical Runge–Kutta method, and Section 3 details its convergence and stability. In Section 4, the Eyring-Prandtl nanofluid flow across a Riga plate is formulated in detail, accounting for electromagnetic forcing, Brownian motion, and thermophoresis on the velocity, temperature, and concentration profiles. The implementation of the scheme on benchmark problems and its validation against exact and MATLAB PDE solver solutions is discussed in Section 5. In Section 6, a neural network-based surrogate model is developed and trained using simulation data to predict the skin friction coefficient and local Sherwood number with high accuracy. Visualization of velocity, temperature, concentration distributions, error contours, and AI regression plots is presented in Section 6 to support the findings. Finally, Section 7 offers concluding remarks, summarising the key insights and highlighting the practical relevance of the proposed hybrid computational-intelligent framework for real-time prediction of non-Newtonian nanofluid transport phenomena.

2 Proposed Predictor Corrector Scheme

A numerical scheme is constructed for discretizing time-dependent partial differential equations. The scheme only discretizes time-dependent terms. The first two stages of the scheme are called predictor stages, while the last stage is called the corrector stage. Before applying a scheme to a differential equation domain, the domain is divided into a finite number of equal subintervals. The solution will be found at the point of each subinterval. We split the domain into a space grid and a time grid: Space: $y \in [0, L]$, divided into $N_y - 1$ equal subintervals, grid points y_j, spacing Δy. Time: $t \in [0, t_f]$, divided into $N_t - 1$ equal time steps, grid points t^n, step size Δt. We will compute approximations: $v_j^n \approx v(t^n, y_j)$. The differential equation can be expressed as:

$$\frac{\partial v}{\partial t} = \alpha_1 \frac{\partial v}{\partial y} + \alpha_2 \frac{\partial^2 v}{\partial y^2}. \tag{1}$$

Subject to the boundary conditions

$$v(t, 0) = f_1(t), v(t, L) = f_2(t). \tag{2}$$

The initial condition is expressed as

$$v(0, y) = f_3(y), \tag{3}$$

where f_1, f_2, f_3 are functions, $v(t, y)$ could be velocity, temperature, or concentration, depending on the physical problem, $\alpha_1 \frac{\partial v}{\partial y}$ is a convection (advection) term: transport due to bulk motion (e.g., fluid moving along a plate) and $\alpha_2 \frac{\partial^2 v}{\partial y^2}$ is a diffusion term: smoothing due to molecular/Brownian diffusion or viscous effects. So, we are essentially designing a scheme that can accurately track how velocity or concentration evolves over time and space under combined convection–diffusion effects.

2.1 Stage 1: Exponential-Type Predictor

The first Stage of the proposed scheme is expressed as:

$$\bar{\boldsymbol{v}}_j^{n+1} = \frac{1}{2}\boldsymbol{v}_j^n e^{2\Delta t} + \frac{1}{2}\boldsymbol{v}_j^n e^{-2\Delta t} + \left(e^{2\Delta t} + e^{-\Delta t} - 2\right)\left\{\frac{\partial \boldsymbol{v}}{\partial t}\bigg|_j^n - \frac{1}{2}\boldsymbol{v}_j^n\right\}. \tag{4}$$

This scheme is first-order accurate in time. This is an exponential integrator-type step. It uses information at time level n: v_j^n, $\frac{\partial v}{\partial t}\big|_j^n$ (which itself depends on spatial derivatives). It's first-order accurate in time and used as a cheap predictor. Stage 1 provides a fast, rough forecast of how the field (velocity, concentration) will evolve over the next time step, accounting for the current local time derivative.

Physical Significance of Eq. (4): Eq. (4) represents the first-stage exponential predictor in the proposed three-stage time integration scheme. This step provides a computationally inexpensive, explicit forecast of the solution at the next time level using the known values of the solution and its time derivative at the current time level n. It belongs to the family of exponential integrators, which are particularly useful in stiff PDEs (e.g., magneto-convective non-Newtonian flows) where conventional explicit methods may require impractically small time steps. The exponential terms in Eq. (4) are introduced to enhance stability and accuracy beyond that of a standard forward Euler predictor. This formulation approximates the temporal evolution in a nonlinear system more accurately when the PDE contains sharp gradients or strong source terms (e.g., electromagnetic force or viscous dissipation).

2.2 Stage 2: Improved Predictor

The second Stage of the scheme is given as:

$$\bar{\bar{\boldsymbol{v}}}_j^{n+1} = a\boldsymbol{v}_j^n + b\bar{\boldsymbol{v}}_j^{n+1} + \frac{1}{4}\Delta t\,\frac{\partial \bar{\boldsymbol{v}}}{\partial t}\bigg|_j^{n+1}. \tag{5}$$

It combines the old solution v_j^n and the first predictor $\bar{v}_j^{n+1}$ and uses a new time derivative $\frac{\partial \bar{v}}{\partial t}$ evaluated at time $n+1$ (but with the predictor). The coefficients a, b are not arbitrary; they will be chosen (with c, d) to enforce third-order accuracy via Taylor Expansion. Stage 2 refines the forecast using improved information about how the PDE responds at the new time level, which is important in systems where the dynamics are sensitive (e.g., strong shear, strong diffusion, electromagnetic forcing).

2.3 Stage 3: Corrector

The last Stage of the scheme is expressed as:

$$v_j^{n+1} = cv_j^n + d\bar{\bar{v}}_j^{n+1} + \frac{2}{3}\Delta t\,\frac{\partial \bar{\bar{v}}}{\partial t}\bigg|_j^{n+1}. \tag{6}$$

This step corrects the solution using the original state v_j^n, the improved predictor $\bar{\bar{v}}_j^{n+1}$, and the updated time derivative. Again, c, d are chosen so that the final scheme matches the Taylor series of the exact solution up to $O(\Delta t^3)$. For our nanofluid flow, it ensures that boundary-layer development, velocity gradients, and concentration gradients are accurately tracked over time. This accuracy is crucial when we compute skin friction and Sherwood number, which depend on derivatives at the wall. The unknown parameters $a, b, c,$

and d will be determined by applying the Taylor series Expansion. For doing this, substitute the first stage (4) into the second stage of the scheme (5) as:

$$\bar{\bar{v}}_j^{n+1} = av_j^n + b\left[\frac{1}{2}v_j^n e^{2\Delta t} + \frac{1}{2}v_j^n e^{-2\Delta t} + \left(e^{2\Delta t} + e^{-\Delta t} - 2\right)\left\{\left.\frac{\partial v}{\partial t}\right|_j^n - \frac{1}{2}v_j^n\right\}\right] + \frac{1}{4}\Delta t$$
$$\left[\frac{1}{2}e^{2\Delta t}\left.\frac{\partial v}{\partial t}\right|_j^n + \frac{1}{2}e^{-2\Delta t}\left.\frac{\partial v}{\partial t}\right|_j^n + \left(e^{2\Delta t} + e^{-\Delta t} - 2\right)\left\{\left.\frac{\partial^2 v}{\partial t^2}\right|_j^n - \frac{1}{2}\left.\frac{\partial v}{\partial t}\right|_j^n\right\}\right]. \tag{7}$$

Eq. (7) can be expressed as

$$\bar{\bar{v}}_j^{n+1} = (a+b)v_j^n + b\left(e^{2\Delta t} + e^{-\Delta t} - 2\right)\left.\frac{\partial v}{\partial t}\right|_j^n + \frac{1}{4}\Delta t\left\{\left.\frac{\partial v}{\partial t}\right|_j^n + \left(e^{2\Delta t} + e^{-\Delta t} - 2\right)\left.\frac{\partial^2 v}{\partial t^2}\right|_j^n\right\}. \tag{8}$$

By putting Eq. (8) into Eq. (6), it yields

$$v_j^{n+1} = cv_j^n + d\left[(a+b)v_j^n + b\left(e^{2\Delta t} + e^{-\Delta t} - 2\right)\left.\frac{\partial v}{\partial t}\right|_j^n + \frac{1}{4}\Delta t\left\{\left.\frac{\partial v}{\partial t}\right|_j^n + \left(e^{2\Delta t} + e^{-\Delta t} - 2\right)\left.\frac{\partial^2 v}{\partial t^2}\right|_j^n\right\}\right]$$
$$+ \frac{2}{3}\Delta t\left[(a+b)\left.\frac{\partial v}{\partial t}\right|_j^n + b\left(e^{2\Delta t} + e^{-\Delta t} - 2\right)\left.\frac{\partial^2 v}{\partial t^2}\right|_j^n + \frac{1}{4}\Delta t\left\{\left.\frac{\partial^2 v}{\partial t^2}\right|_j^n + \left(e^{2\Delta t} + e^{-\Delta t} - 2\right)\left.\frac{\partial^3 v}{\partial t^3}\right|_j^n\right\}\right]. \tag{9}$$

Rewrite Eq. (9) as

$$v_j^{n+1} = [c + d(a+b)]v_j^n + \left[bd\left(e^{2\Delta t} + e^{-\Delta t} - 2\right) + \frac{d}{4}\Delta t + \frac{2}{3}\Delta t(a+b)\right]\left.\frac{\partial v}{\partial t}\right|_j^n$$
$$+ \left[\frac{d\Delta t}{4}\left(e^{2\Delta t} + e^{-\Delta t} - 2\right) + \frac{2b}{3}\Delta t\left(e^{2\Delta t} + e^{-\Delta t} - 2\right) + \frac{(\Delta t)^2}{6}\left.\frac{\partial^2 v}{\partial t^2}\right|_j^n\right]$$
$$+ \left[\frac{(\Delta t)^2}{6}\left(e^{2\Delta t} + e^{-\Delta t} - 2\right)\left.\frac{\partial^3 v}{\partial t^3}\right|_j^n\right]. \tag{10}$$

Now expanding v_j^{n+1} using the Taylor series as

$$v_j^{n+1} = v_j^n + \Delta t\left.\frac{\partial v}{\partial t}\right|_j^n + \frac{(\Delta t)^2}{2}\left.\frac{\partial^2 v}{\partial t^2}\right|_j^n + \frac{(\Delta t)^3}{6}\left.\frac{\partial^3 v}{\partial t^3}\right|_j^n + O\left((\Delta t)^4\right). \tag{11}$$

Using Taylor series Expansion (11) in Eq. (10) and comparing the coefficients of v_j^n, $\left.\frac{\partial v}{\partial t}\right|_j^n$, $\left.\frac{\partial^2 v}{\partial t^2}\right|_j^n$ and $\left.\frac{\partial^3 v}{\partial t^3}\right|_j^n$ on both sides of the resulting equations, it gives

$$\left.\begin{array}{l} c + d(a+b) = 1 \\ bd\left(e^{2\Delta t} + e^{-\Delta t} - 2\right) + \frac{d}{4}\Delta t + \frac{2}{3}\Delta t(a+b) = \Delta t \\ \frac{d\Delta t}{4}\left(e^{2\Delta t} + e^{-\Delta t} - 2\right) + \frac{2b}{3}\Delta t\left(e^{2\Delta t} + e^{-\Delta t} - 2\right) + \frac{(\Delta t)^2}{6} = \frac{(\Delta t)^2}{2} \\ \frac{(\Delta t)^2}{6}\left(e^{2\Delta t} + e^{-\Delta t} - 2\right) = \frac{(\Delta t)^3}{6} \end{array}\right\}. \tag{12}$$

Solving a system of Eq. (12) yields

$a = \frac{1}{16}\left(16 - 12d + 9d^2\right), b = \frac{1}{8}\left(4 - 3d\right), c = \frac{1}{16}(16 - 24d + 18d^2 - 9d^3)$ and d is a free parameter. This matching guarantees that, for reasonably smooth solutions, the method is third-order accurate in time, meaning that the time integration error is very small even for moderately large Δt. This is particularly valuable for stiff problems such as non-Newtonian MHD flows, where simple explicit schemes require extremely small time steps to remain stable.

2.4 Compact Spatial Discretization

Up to now, we treated $\frac{\partial v}{\partial t}$ as if we know it exactly. In practice, $\frac{\partial v}{\partial t}\Big|_j^n = \alpha_1 \frac{\partial v}{\partial t}\Big|_j^n + \alpha_2 \frac{\partial^2 v}{\partial y^2}\Big|_j^n$. Since the proposed scheme discretizes only the time derivative in Eq. (1), a compact scheme is employed for space discretization. Therefore, the proposed scheme using compact spatial discretization is given as

$$\overline{v}_j^{n+1} = \frac{1}{2}v_j^n e^{2\Delta t} + \frac{1}{2}v_j^n e^{-\Delta t} + \left(e^{2\Delta t} + e^{-\Delta t} - 2\right)\left\{\alpha_1 A_1^{-1} B_1 v_j^n + \alpha_2 A_2^{-1} B_2 v_j^n - \frac{1}{2}v_j^n\right\}, \tag{13}$$

$$\overline{\overline{v}}_j^{n+1} = a v_j^n + b\overline{v}_j^{n+1} + \frac{1}{4}\Delta t\left\{\alpha_1 A_1^{-1} B_1 \overline{v}_j^{n+1} + \alpha_2 A_2^{-1} B_2 \overline{v}_j^{n+1}\right\}, \tag{14}$$

$$v_j^{n+1} = c v_j^n + d\overline{\overline{v}}_j^{n+1} + \frac{2}{3}\Delta t\left\{\alpha_1 A_1^{-1} B_1 \overline{\overline{v}}_j^{n+1} + \alpha_2 A_2^{-1} B_2 \overline{\overline{v}}_j^{n+1}\right\}, \tag{15}$$

where A_1, A_2 and B_1, B_2 are matrices that are constructed from the left-hand and right-hand sides of the following equations, respectively.

For first derivative:

$$\beta_1\, v'|_{j+1}^n + v'|_i^n + \beta_1\, v'|_{j-1}^n = b_\circ \frac{(v_{j+1}^n - v_{j-1}^n)}{2\Delta y} + b_1 \frac{(v_{j+2}^n - v_{j-2}^n)}{4\Delta y}. \tag{16}$$

For the second derivative:

$$\beta_2\, v''|_{j+1}^n + v''|_j^n + \beta_2\, v''|_{j-1}^n = b_2 \frac{(v_{j+1}^n - 2v_j^n + v_{j-1}^n)}{(\Delta y)^2} + b_3 \frac{(v_{j+2}^n - 2v_j^n + v_{j-2}^n)}{4\,(\Delta y)^2}. \tag{17}$$

where $b_\circ = \frac{2}{3}\left(\beta_1 + 2\right), b_1 = \frac{1}{3}\left(-4\beta_1 + 1\right), b_2 = \frac{4}{3}\left(1 - \beta_2\right), b_3 = \frac{1}{3}(10\beta_2 - 1)$.

These relations can be written in matrix form: $A_1 v_y = B_1 v$, so $v_y \approx A_1^{-1} B_1 v$. $A_2 v_{yy} = B_2 v$, so $v_{yy} \approx A_2^{-1} B_2 v$. So, in our final scheme: $\frac{\partial v}{\partial t}\Big|_j^n \approx \alpha_1 A_1^{-1} B_1 v^n + \alpha_2 A_2^{-1} B_2 v^n$.

This scheme gives a higher-order spatial accuracy using short stencils (involving only a few neighbouring points). It captures sharp gradients better, which is essential when we calculate wall shear stress (forskin friction) and the wall concentration gradient (for the Sherwood number).

3 Stability and Convergence Analysis

To determine the necessary conditions for the stability of finite difference schemes, authors have used either the von Neumann or the Fourier series stability analyses. The analysis transforms the difference equations into a trigonometric equation. The analysis considers both time- and space-discretization schemes. It gives exact stability conditions of finite difference schemes applied to a linear differential equation. It may apply to a non-linear differential equation after linearization. For non-linear differential equations, it provides an estimate of the exact stability conditions. The transformations for this case can be expressed as:

$$A_1 e^{iI\psi} = \beta_1 e^{(j+1)i\psi} + e^{iI\psi} + \beta_1 e^{(j-1)i\psi}, \tag{18}$$

$$B_1 e^{iI\psi} = b_\circ \frac{\left(e^{(j+1)i\psi} - e^{(j-1)I\psi}\right)}{2\Delta y} + b_1 \frac{\left(e^{(j+2)i\psi} - e^{(j-2)i\psi}\right)}{4\Delta y}, \tag{19}$$

$$A_2 e^{iI\psi} = \beta_2 e^{(j+1)i\psi} + e^{iI\psi} + \beta_2 e^{(j-1)i\psi}, \tag{20}$$

$$B_2 e^{iI\psi} = b_2 \frac{\left(e^{(j+1)i\psi} - 2e^{iI\psi} + e^{(j-1)i\psi}\right)}{(\Delta y)^2} + b_3 \frac{\left(e^{(j+2)i\psi} - 2e^{iI\psi} + e^{(j-2)i\psi}\right)}{4(\Delta y)^2}, \tag{21}$$

where $i = \sqrt{-1}$ is an imaginary number.

Using transformations (18)–(21) into the first stage of the proposed scheme (13) gives

$$\begin{aligned}\overline{v}_j^{n+1} &= \frac{1}{2} v_i^n e^{2\Delta t} + \frac{1}{2} v_i^n e^{-\Delta t} \\ &+ \left(e^{2\Delta t} + e^{-\Delta t} - 2\right)\left\{\alpha_1\left(\frac{2b_\circ isin\psi + b_1 isin2\psi}{2\Delta y\left(2\beta_1 \cos\psi + 1\right)}\right) + \alpha_2\left(\frac{4b_2(cos\psi - 1) + b_3(cos2\psi - 1)}{2(\Delta y)^2\left(2\beta_2 \cos\psi + 1\right)}\right) - \frac{1}{2}\right\} v_j^n.\end{aligned} \tag{22}$$

Eq. (22) can be re-written as

$$\overline{v}_j^{n+1} = \left(c_1 + ic_2\right) v_j^n, \tag{23}$$

where $c_1 = \frac{1}{2}e^{2\Delta t} + \frac{1}{2}e^{-\Delta t} + \left(e^{2\Delta t} + e^{-\Delta t} - 2\right)\left\{\alpha_2\left(\frac{4b_2(cos\psi-1)+b_3(cos2\psi-1)}{2(\Delta y)^2(2\beta_2 \cos\psi+1)}\right) - \frac{1}{2}\right\}$.

And $c_2 = \left(e^{2\Delta t} + e^{-\Delta t} - 2\right)\left\{\alpha_1\left(\frac{2b_\circ sin\psi + b_1 sin2\psi}{2\Delta y(2\beta_1 \cos\psi+1)}\right)\right\}$.

Now using transformations (18)–(21) into the second stage of the scheme (14) yields.

$$\overline{\overline{v}}_j^{n+1} = av_j^n + b\overline{v}_j^{n+1} + \frac{1}{4}\Delta t\left\{\alpha_1\left(\frac{2b_\circ isin\psi + b_1 isin2\psi}{2\Delta y\left(2\beta_1 \cos\psi + 1\right)}\right) + \alpha_2\left(\frac{4b_2(cos\psi - 1) + b_3(cos2\psi - 1)}{2(\Delta y)^2\left(2\beta_2 \cos\psi + 1\right)}\right)\right\}\overline{v}_j^{n+1}. \tag{24}$$

Rewrite Eq. (24) as

$$\overline{\overline{v}}_j^{n+1} = av_j^n + \left(c_3 + ic_4\right)\overline{v}_j^{n+1}, \tag{25}$$

where $c_3 = b + \frac{1}{4}\Delta t\alpha_1\left(\frac{2b_\circ sin\psi + b_1 sin2\psi}{2\Delta y(2\beta_1 \cos\psi+1)}\right)$ and $c_4 = \frac{1}{4}\Delta t\alpha_2\left(\frac{4b_2(cos\psi-1)+b_3(cos2\psi-1)}{2(\Delta y)^2(2\beta_2 \cos\psi+1)}\right)$.

Substituting Eq. (23) into Eq. (25) leads to

$$\overline{\overline{v}}_j^{n+1} = \left(c_5 + ic_6\right) v_j^n, \tag{26}$$

where $c_5 = a + c_1c_3 - c_2c_4$ and $c_6 = c_1c_4 + c_2c_3$.

Now using transformations (18)–(21) into the third stage of the scheme (15) is

$$v_j^{n+1} = cv_j^n + \left(c_7 + ic_8\right)\overline{\overline{v}}_j^{n+1}. \tag{27}$$

Substituting Eq. (26) into Eq. (27) yields

$$v_j^{n+1} = \left(c_9 + ic_{10}\right) v_j^n, \tag{28}$$

where $c_9 = c + c_5c_7 - c_6c_8$ and $c_{10} = c_5c_8 + c_6c_7$,

where $c_7 = d + \frac{2\Delta t}{3}\alpha_1\left(\frac{2b_o sin\psi + b_1 sin2\psi}{2\Delta y(2\beta_1 \cos\psi + 1)}\right)$ and $c_8 = \frac{2\Delta t}{3}\alpha_2\left(\frac{4b_2(cos\psi - 1) + b_3(cos2\psi - 1)}{2(\Delta y)^2(2\beta_2 \cos\psi + 1)}\right)$

The amplification factor for this case is written as

$$\frac{v_j^{n+1}}{v_j^n} = c_9 + ic_{10}. \tag{29}$$

The scheme will be stable if

$$\left|\frac{v_j^{n+1}}{v_j^n}\right|^2 \leq 1. \tag{30}$$

Which gives the stability conditions $c_9^2 + c_{10}^2 \leq 1$. If the scheme satisfies this condition, it will remain stable; otherwise, an unstable solution will be obtained. The stability condition is found for a scalar convection-diffusion problem.

To find the convergence condition for the system of convection diffusion equations, consider the following equation.

$$\frac{\partial \boldsymbol{P}}{\partial t} = \overline{A}_1\frac{\partial \boldsymbol{P}}{\partial y} + \overline{A}_2\frac{\partial^2 \boldsymbol{P}}{\partial y^2}. \tag{31}$$

where $\boldsymbol{P}$ is a vector and $\overline{A}_1, \overline{A}_2$ are matrices. The proposed scheme, when applied to Eq. (31), takes the form

$$\overline{\boldsymbol{P}}_j^{n+1} = \frac{1}{2}\boldsymbol{P}_j^n e^{2\Delta t} + \frac{1}{2}\boldsymbol{P}_j^n e^{-\Delta t} + \left(e^{2\Delta t} + e^{-\Delta t} - 2\right)\left\{\overline{A}_1 A_1^{-1} B_1 \boldsymbol{P}_j^n + \overline{A}_2 A_2^{-1} B_2 \boldsymbol{P}_j^n - \frac{1}{2}\boldsymbol{P}_j^n\right\}, \tag{32}$$

$$\overline{\overline{\boldsymbol{P}}}_j^{n+1} = a\boldsymbol{P}_j^n + b\overline{\boldsymbol{P}}_j^{n+1} + \frac{1}{4}\Delta t\left\{\overline{A}_1 A_1^{-1} B_1 \overline{\boldsymbol{P}}_j^{n+1} + \overline{A}_2 A_2^{-1} B_2 \overline{\boldsymbol{P}}_j^{n+1}\right\}, \tag{33}$$

$$\boldsymbol{P}_j^{n+1} = c\boldsymbol{P}_j^n + d\overline{\overline{\boldsymbol{P}}}_j^{n+1} + \frac{2}{3}\Delta t\left\{\overline{A}_1 A_1^{-1} B_1 \overline{\overline{\boldsymbol{P}}}_j^{n+1} + \overline{A}_2 A_2^{-1} B_2 \overline{\overline{\boldsymbol{P}}}_j^{n+1}\right\}. \tag{34}$$

Theorem: *The proposed scheme (32)–(34) converges conditionally for the vectored matrix Eq. (31).*

Proof: To prove this Theorem, consider the first stage of the exact scheme as:

$$\overline{\boldsymbol{P}}_j^{n+1} = \frac{1}{2}\boldsymbol{P}_j^n e^{2\Delta t} + \frac{1}{2}\boldsymbol{P}_j^n e^{-\Delta t} + \left(e^{2\Delta t} + e^{-\Delta t} - 2\right)\left\{\overline{A}_1 A_1^{-1} B_1 \boldsymbol{P}_j^n + \overline{A}_2 A_2^{-1} B_2 \boldsymbol{P}_j^n - \frac{1}{2}\boldsymbol{P}_j^n\right\}. \tag{35}$$

Subtracting the first stage of the proposed and exact scheme, and let $\boldsymbol{P}_j^n - \boldsymbol{p}_j^n = \boldsymbol{E}_j^n$, etc., it yields

$$\overline{\boldsymbol{E}}_j^{n+1} = \frac{1}{2}\boldsymbol{E}_j^n e^{2\Delta t} + \frac{1}{2}\boldsymbol{E}_j^n e^{-\Delta t} + \left(e^{2\Delta t} + e^{-\Delta t} - 2\right)\left\{\overline{A}_1 A_1^{-1} B_1 \boldsymbol{E}_j^n + \overline{A}_2 A_2^{-1} B_2 \boldsymbol{E}_j^n - \frac{1}{2}\boldsymbol{E}_j^n\right\}. \tag{36}$$

Applying the norm $\|\cdot\|_\infty$ on both sides of Eq. (36) that yields

$$\overline{E}^{n+1} \leq \frac{1}{2}E^n e^{2\Delta t} + \frac{1}{2}E^n e^{-\Delta t} + \left(e^{2\Delta t} + e^{-\Delta t} - 2\right)\left\{\left\|\overline{A}_1 A_1^{-1} B_1\right\|_\infty E^n + \left\|\overline{A}_2 A_2^{-1} B_2\right\|_\infty E^n + \frac{1}{2}E^n\right\}. \tag{37}$$

Inequality (37) can be rewritten as

$$\overline{E}^{n+1} \leq \gamma_1 E^n, \tag{38}$$

where $\gamma_1 = \frac{1}{2}e^{2\Delta t} + \frac{1}{2}e^{-\Delta t} + \left(e^{2\Delta t} + e^{-\Delta t} - 2\right)\left\{\left\|\overline{A}_1 A_1^{-1} B_1\right\|_\infty + \left\|\overline{A}_2 A_2^{-1} B_2\right\|_\infty\right\}$.

The second stage of the exact scheme for Eq. (31) is written as

$$\overset{=}{\boldsymbol{P}}_j^{n+1} = a\boldsymbol{P}_j^n + b\overline{\boldsymbol{P}}_j^{n+1} + \frac{1}{4}\Delta t\left\{\overline{A}_1 A_1^{-1} B_1 \overline{\boldsymbol{P}}_j^{n+1} + \overline{A}_2 A_2^{-1} B_2 \overline{\boldsymbol{P}}_j^{n+1}\right\}. \tag{39}$$

The corresponding error equation is expressed as

$$\overset{=}{\boldsymbol{E}}_j^{n+1} = a\boldsymbol{E}_j^n + b\overline{\boldsymbol{E}}_j^{n+1} + \frac{1}{4}\Delta t\left\{\overline{A}_1 A_1^{-1} B_1 \overline{\boldsymbol{E}}_j^{n+1} + \overline{A}_2 A_2^{-1} B_2 \overline{\boldsymbol{E}}_j^{n+1}\right\}. \tag{40}$$

Applying the norm $\|\cdot\|_\infty$ on both sides of Eq. (40) as

$$\overset{=}{E}^{n+1} \le aE^n + b\overline{E}^{n+1} + \frac{1}{4}\Delta t\left\{\left\|\overline{A}_1 A_1^{-1} B_1\right\|_\infty \overline{E}^{n+1} + \left\|\overline{A}_2 A_2^{-1} B_2\right\|_\infty \overline{E}^{n+1}\right\}. \tag{41}$$

Rewrite inequality (41) as

$$\overset{=}{E}^{n+1} \le aE^n + \gamma_2 \overline{E}^{n+1}. \tag{42}$$

where $\gamma_2 = b + \frac{1}{4}\Delta t\left\{\left\|\overline{A}_1 A_1^{-1} B_1\right\|_\infty + \left\|\overline{A}_2 A_2^{-1} B_2\right\|_\infty\right\}$.

Substituting inequality (38) into inequality (42) results in

$$\overset{=}{E}^{n+1} \le \gamma_3 E^n, \tag{43}$$

where $\gamma_3 = a + \gamma_1\gamma_2$.

The third stage of the exact scheme can be written as

$$\boldsymbol{P}_j^{n+1} = c\boldsymbol{P}_j^n + d\overline{\overline{\boldsymbol{P}}}_j^{n+1} + \frac{2}{3}\Delta t\left\{\overline{A}_1 A_1^{-1} B_1 \overline{\overline{\boldsymbol{P}}}_j^{n+1} + \overline{A}_2 A_2^{-1} B_2 \overline{\overline{\boldsymbol{P}}}_j^{n+1}\right\}. \tag{44}$$

The error equation corresponding to Eq. (44) is

$$\boldsymbol{E}_j^{n+1} = c\boldsymbol{E}_j^n + d\overline{\overline{\boldsymbol{E}}}_j^{n+1} + \frac{2}{3}\Delta t\left\{\overline{A}_1 A_1^{-1} B_1 \overline{\overline{\boldsymbol{E}}}_j^{n+1} + \overline{A}_2 A_2^{-1} B_2 \overline{\overline{\boldsymbol{E}}}_j^{n+1}\right\}. \tag{45}$$

Applying the norm $\|\cdot\|_\infty$ on both sides of Eq. (45) as

$$E^{n+1} \le cE^n + d\overset{=}{E}^{n+1} + \frac{2}{3}\Delta t\left\{\left\|\overline{A}_1 A_1^{-1} B_1\right\|_\infty + \left\|\overline{A}_2 A_2^{-1} B_2\right\|_\infty\right\}\overset{=}{E}^{n+1}. \tag{46}$$

Rewrite inequality (46) as

$$E^{n+1} \le cE^n + \gamma_4 \overset{=}{E}^{n+1} + N\left(O\left((\Delta t)^3, (\Delta y)^6\right)\right), \tag{47}$$

where $\gamma_4 = d + \frac{2}{3}\Delta t\left\{\left\|\overline{A}_1 A_1^{-1} B_1\right\|_\infty + \left\|\overline{A}_2 A_2^{-1} B_2\right\|_\infty\right\}$.

Using inequality (43) in inequality (47) as

$$E^{n+1} \le \gamma_5 E^n + N\left(O\left((\Delta t)^3, (\Delta y)^6\right)\right), \tag{48}$$

where $\gamma_5 = c + \gamma_3\gamma_4$.

Let $n = 0$ in inequality (48), which yields

$$E^1 \leq \gamma_5 E^0 + N\left(O\left((\Delta t)^3, (\Delta y)^6\right)\right). \tag{49}$$

Since $E^0 = 0$, so inequality (49) becomes

$$E^1 \leq N\left(O\left((\Delta t)^3, (\Delta y)^6\right)\right). \tag{50}$$

Let $n = 1$ in inequality (48), which results in

$$E^2 \leq \gamma_5 E^1 + N\left(O\left((\Delta t)^3, (\Delta y)^6\right)\right). \tag{51}$$

Using inequality (50) in inequality (51) gives

$$E^2 \leq (1 + \gamma_5) + N\left(O\left((\Delta t)^3, (\Delta y)^6\right)\right). \tag{52}$$

If this continued, then for finite n

$$E^n \leq \left(1 + \gamma_5 + \ldots + \gamma_5^{n-1}\right) N\left(O\left((\Delta t)^3, (\Delta y)^6\right)\right) = \left(\frac{1-\gamma_5^n}{1-\gamma}\right) N\left(O\left((\Delta t)^3, (\Delta y)^6\right)\right). \tag{53}$$

By taking $limit$as $n \to \infty$ the infinite series $\ldots + \gamma_5^n + \ldots + \gamma_5 + 1$ is a finite geometric series that converges if $|\gamma_5| < 1$.□

4 Problem Statement

Consider one-dimensional, unsteady, laminar, incompressible, homogeneous in the x^*-direction (i.e., $\frac{\partial}{\partial x} = 0$) Eyring-Prandtl nano fluid flow over Riga plate. The Riga plate comprises an array of electrodes and magnets that generate a steady Lorentz force acting tangentially to the fluid. Let x^*-axis is placed vertically and y^*-axis is perpendicular to it. The Riga plate lies along x^*-axis parallel to x^*-axis. The fluid occupies the region $y^* > 0$. Let the plate suddenly move along the positive x^*-axis. A slip boundary condition is imposed at the wall. Let T_w and C_w are temperature and nanoparticle concentration at the plate. Ambient temperature and nanoparticle concentration are far away from the plate and are denoted, respectively, by T_∞ and C_∞.

Model Assumptions and Coordinate System: A Cartesian coordinate system is used: x^*-axis is aligned vertically along the plate (direction of flow). y^*-axis is normal to the plate, pointing into the fluid domain. The flow is assumed to be: Unsteady, i.e., velocity, temperature, and concentration vary with time. Incompressible, meaning the fluid density is constant. Laminar and one-dimensional in the y^*-direction; all $\partial/\partial x = 0$. Homogeneous and Newtonian in bulk, but governed by the Eyring-Prandtl non-Newtonian viscosity model. The fluid is: A nanofluid, i.e., a base fluid containing suspended nanoparticles. Electrically conducting and influenced by electromagnetic forces generated by the Riga plate. The Riga plate is: A surface embedded with alternating magnets and electrodes that produce a steady Lorentz force along the x^*-direction. Subject to a velocity slip boundary condition, rather than a no-slip. Heat and mass transfer considerations include: Thermophoresis and Brownian motion effects (key features of nanofluid dynamics). Viscous dissipation due to Eyring–Prandtl fluid behavior. A chemical reaction term acting as a sink in the energy and concentration equations. The ambient conditions are: Far from the plate, fluid is at rest, and at ambient temperature T_∞ and concentration C_∞. Additional assumptions: No external pressure gradient is imposed. Constant thermal

conductivity and mass diffusivity. The governing equations are written under dimensional and dimensionless forms to facilitate analysis. The governing equations are expressed as:

$$\frac{\partial u^*}{\partial t^*} = \frac{\overline{\beta}}{\overline{C}}\left(\frac{\frac{\partial^2 u^*}{\partial y^{*2}}}{\sqrt{1+\left(\frac{1}{\overline{C}}\frac{\partial u^*}{\partial y^*}\right)^2}}\right) + g\beta_T\left(T-T_\infty\right) + g\beta_C\left(C-C_\infty\right) + \frac{\pi j_\circ M_\circ}{8\rho}\exp\left(-\frac{\pi y^*}{a_1}\right), \tag{54}$$

$$\frac{\partial T}{\partial t^*} = \alpha\frac{\partial^2 T}{\partial y^{*2}} + \frac{\overline{\beta}}{\rho C_p}\sinh^{-1}\left(\frac{1}{\overline{C}}\frac{\partial u^*}{\partial y^*}\right)\frac{\partial u^*}{\partial y^*} + \tau\left(D_B\frac{\partial C}{\partial y^*}\frac{\partial T}{\partial y^*} + \frac{D_T}{T_\infty}\left(\frac{\partial T}{\partial y^*}\right)^2\right) - k_1\left(C-C_\infty\right), \tag{55}$$

$$\frac{\partial C}{\partial t^*} = D_B\frac{\partial^2 C}{\partial y^{*2}} + \frac{D_T}{T_\infty}\frac{\partial^2 T}{\partial y^{*2}}. \tag{56}$$

Momentum Eq. (54) (x^*-direction): $\frac{\partial u^*}{\partial t^*}$ represents an unsteady change in velocity; it tracks how the fluid accelerates or decelerates over time. $\frac{\partial^2 u^*}{\partial y^{*2}}$ is the Momentum diffusion (viscous force) in y^*-direction, it captures the spread of velocity due to internal friction. $\sqrt{1+\left(\frac{1}{\overline{C}}\frac{\partial u^*}{\partial y^*}\right)^2}$ represents the Eyring–Prandtl nonlinearity (shear-thinning), it models how viscosity varies with shear, common in polymers, biofluids, etc. $\frac{\overline{\beta}}{\overline{C}}$ is the stress scale from the Eyring–Prandtl model controls how strongly the fluid resists deformation. $g\beta_T\left(T-T_\infty\right)$ and $g\beta_C\left(C-C_\infty\right)$ are the thermal and Solutal buoyancy forces, respectively. $\frac{\pi j_\circ M_\circ}{8\rho}e^{-\left(\frac{\pi}{a_1}\right)y^*}$ is the Lorentz force (electromagnetic) from the Riga plate, it drives the fluid forward along the wall with exponentially decaying intensity. The Eyring–Prandtl term captures non-Newtonian shear-thinning behavior in smart fluids, slurries, and synthetic lubricants. Buoyancy terms are important in free-convection nanofluid flows, e.g., in cooling devices or bioconvection, and the Riga plate force is the main driver of the flow, representing active electromagnetic pumping used in microfluidics, MHD accelerators, or coating technologies.

Energy Eq. (55): $\frac{\partial T}{\partial t^*}$ represents the rate of change of temperature, also referred to as unsteady heat conduction, $\alpha\frac{\partial^2 T}{\partial y^{*2}}$ is the Thermal diffusion spreads heat within the fluid, $\frac{\overline{\beta}}{\rho C_p}\sinh^{-1}\left(\frac{1}{\overline{C}}\frac{\partial u^*}{\partial y^*}\right)\frac{\partial u^*}{\partial y^*}$ is the viscous dissipation (frictional heating), it converts mechanical work into thermal energy, $\tau D_B\frac{\partial C}{\partial y^*}\frac{\partial T}{\partial y^*}$ is the Brownian-motion-induced coupling, which affects heat due to nanoparticle concentration gradients, $\tau\frac{D_T}{T_\infty}\left(\frac{\partial T}{\partial y^*}\right)^2$ is the Thermophoresis effect, when nanoparticles migrate from hot to cold regions, affecting the thermal field and $-k_1(C-C_\infty)$ represents the Energy sink due to a chemical reaction; it removes heat from exothermic or endothermic processes.

Nanoparticle Concentration Eq. (56): $\frac{\partial C}{\partial t^*}$ represents the rate of change of nanoparticle concentration, it captures nanoparticle transport over time, $D_B\frac{\partial^2 C}{\partial y^{*2}}$ is the Mass diffusion (Brownian motion), in a random motion of particles, increases the spread and $\frac{D_T}{T_\infty}\frac{\partial^2 T}{\partial y^{*2}}$ Thermophoresis (temperature-driven diffusion) causes particles to move from hot to cold areas.

Subject to the following initial and boundary conditions

$$\left.\begin{array}{l} u^* = 0, T = 0, C = 0\, when\, t^* = 0 \\ u^* = u_w + L_s\frac{\partial u^*}{\partial y^*}, T = T_w, C = C_w\, at\, y^* = 0 \\ u^* \to 0, T \to T_\infty, C \to C_\infty\, when\, y^* \to \infty \end{array}\right\}. \tag{57}$$

Physical Significance of initial and Boundary Conditions (Dimensional Form): Initial condition at time $t^* = 0$, the fluid is at rest. It is at ambient temperature and ambient nanoparticle concentration. Boundary conditions at the wall $y^* = 0$, unlike the no-slip condition in classical flows, here: $u^*(t^*, 0) = u_w + L_s \left.\frac{\partial u^*}{\partial y^*}\right|_{y^*=0}$, u_w is the reference wall velocity (often a constant or specified function) and L_s is the slip length, indicating how much fluid slides along the wall. $T = T_w, C = C_w$ is the Dirichlet condition prescribes heat and nanoparticle injection. Far-field conditions as $y^* \to \infty$, far from the plate: The fluid is undisturbed (no motion). It maintains ambient temperature and ambient nanoparticle concentration.

Where u^* is the horizontal component of velocity, $\overline{C}$ is the rate parameter, $\overline{\beta}$ is a stress parameter, $M_\circ$ is a magnetic field strength, $j_\circ$ is current density, a_1 width of electrodes, g is gravity, β_T is thermal Expansion, β_C is solutal Expansion, α is thermal diffusivity, D_B is the Brownian motion coefficient, D_T represents the thermophoresis coefficients, c_p is the specific heat capacity, k_1 is the reaction rate parameter.

Now using transformations

$$\left.\begin{aligned} y = \frac{y^*}{L}, u = \frac{u^*}{u_w}, t = \frac{u_w t^*}{L}, \theta = \frac{T - T_\infty}{T_w - T_\infty}, \phi = \frac{C - C_\infty}{C_w - C_\infty} \end{aligned}\right\}. \tag{58}$$

Dimensionless Transformations Eq. (58): These transformations will normalize the system over characteristic scales: Length scale L, Velocity scale u_w, Temperature and concentration differences. Make the equations dimensionless, introducing key physical parameters.

Using the transformation (58) into the governing Eqs. (54)–(57) results in

$$\frac{\partial u}{\partial t} = \frac{1}{R_e}\left(\frac{\partial^2 u/\partial y^2}{\sqrt{1 + S^2\left(\partial u/\partial y\right)^2}}\right) + \frac{G_{\gamma_L}}{R_e^2}\theta + \frac{G_{\gamma_C}}{R_e^2}\phi + Me^{-\lambda y}, \tag{59}$$

$$\frac{\partial \theta}{\partial t} = \frac{1}{P_r R_e}\frac{\partial^2 \theta}{\partial y^2} + \frac{E_c}{R_e S}\sinh^{-1}\left(\frac{S\partial u}{\partial y}\right)\frac{\partial u}{\partial y} + \frac{N_b}{R_e}\frac{\partial \phi}{\partial y}\frac{\partial \theta}{\partial y} + \frac{N_t}{R_e}\left(\frac{\partial \theta}{\partial y}\right)^2, \tag{60}$$

$$\frac{\partial \phi}{\partial t} = \frac{1}{S_c R_e}\frac{\partial^2 \phi}{\partial y^2} + \frac{N_t}{S_c N_b R_e}\frac{\partial^2 \theta}{\partial y^2} - \gamma\phi. \tag{61}$$

Subject to the dimensionless initial and boundary conditions

$$\left.\begin{aligned} u = \theta = \phi = 0\, for\, t = 0 \\ u = 1 + \Lambda\frac{\partial u}{\partial y}, \theta = 1, \phi = 1 when\, y = 0 \\ u \to 0, \theta \to 0, \phi \to 0\, when\, y \to \infty \end{aligned}\right\}, \tag{62}$$

where M is a dimensionless electromagnetic (Riga) parameter, S is the Eyring (shear) number, R_e Reynolds number, λ is the dimensionless decay rate of the Lorentz force in the y-direction, G_{γ_L} and G_{γ_C} are respectively the thermal and solutal Grashof numbers, P_r is the Prandtl number, E_c is the Eckert number, S_c is Schmidt number, N_b represents the Brownian motion, N_t represents the thermophoresis parameter, γ is a dimensionless reaction rate parameter, and Λ is the velocity slip, which are defined as:

$$M = \frac{\pi j_\circ M_\circ L}{8\rho u_w^2},\ S = \frac{u_w}{L\bar{C}},\ R_e = \frac{\rho u_w L\bar{C}}{\bar{\beta}},\ \lambda = \frac{\pi}{a_1},\ G_{\gamma_L} = \frac{L^3 g\beta_T\left(T_w - T_\infty\right)}{\nu^2},\ G_{\gamma_C} = \frac{g\beta_C\left(C_w - C_\infty\right)}{\nu^2},\ P_r = \frac{\nu}{\alpha},$$

$$E_c = \frac{u_w^2}{C_p\left(T_w - T_\infty\right)},\ N_b = \frac{\tau D_B\left(C_w - C_\infty\right)}{\nu},\ N_t = \frac{\tau D_T\left(T_w - T_\infty\right)}{\nu T_\infty},\ S_c = \frac{\nu}{D_B},\ \gamma = \frac{k_1 L}{u_w},\ \Lambda = \frac{L_s}{L}.$$

The skin friction coefficients, local Nusselt, and local Sherwood numbers are defined as:

$$\left.\begin{aligned} C_f &= \frac{\tau_w}{\rho u_w^2} \\ N_{uL} &= \frac{L q_w}{k(T_w - T_\infty)} \\ S_{h_L} &= \frac{L j_w}{D_B(C_w - C_\infty)} \end{aligned}\right\}, \tag{63}$$

where $\tau_w = \overline{\beta}\sinh^{-1}\left(\frac{1}{\overline{C}}\frac{\partial u^*}{\partial y^*}\right)$, $q_w = -k\left.\frac{\partial T}{\partial y^*}\right|_{y^*=0}$, $j_w = -D_B\left.\frac{\partial C}{\partial y^*}\right|_{y^*=0} - \frac{D_T}{T_\infty}\left.\frac{\partial T}{\partial y^*}\right|_{y^*=0}$. These are the system's engineering performance metrics. Skin friction is the frictional resistance exerted by the fluid on the moving wall and is critical to drag reduction, energy efficiency, and pump power requirements. The Nusselt number represents the rate of convective heat transfer at the wall relative to conduction. High N_{uL}: efficient cooling/heating. The local Sherwood number measures the mass transfer rate at the wall (nanoparticles moving into/out of the fluid). It is crucial for coating, drug delivery, and nano-precipitation systems.

Applying transformation (58) into (63) gives:

$$C_f = \frac{1}{R_e S}\sinh^{-1}\left(S u_y\big|_{y=0}\right), N_{uL} = -\left.\frac{\partial\theta}{\partial y}\right|_{y=0}, S_{h_L} = -\left[\left.\frac{\partial\phi}{\partial y}\right|_{y=0} + \frac{N_t}{N_b}\left.\frac{\partial\theta}{\partial y}\right|_{y=0}\right]. \tag{64}$$

These are the non-dimensional counterparts of Eq. (63), derived using the scaling variables from Eq. (58).

The discretization of Eqs. (59)–(61) using the proposed scheme is given below, with time discretization via a three-stage predictor–corrector scheme (already explained earlier). Spatial derivatives approximated using compact finite difference matrices: $A_1^{-1}B_1$: first derivative (e.g., u_y, θ_y, ϕ_y), $A_2^{-1}B_2$: second derivative (e.g., u_{yy}, θ_{yy}, ϕ_{yy}). The goal is to advance the solution from time level n to $n+1$ using three stages: First-stage predictor: (bar), Second Stage improved predictor:(double bar), and Third-stage corrector: final value at t^{n+1}. These are the discretized forms of the dimensionless governing equations (velocity u, temperature θ, and concentration ϕ) using the three-stage hybrid time integration scheme combined with compact finite-difference spatial operators.

Momentum Equation (Discretized):

First-Stage Predictor for Velocity:

$$\begin{aligned} \overline{u}_j^{n+1} &= \frac{1}{2}u_j^n e^{2\Delta t} + \frac{1}{2}u_j^n e^{-\Delta t} \\ &+ \left(e^{2\Delta t} + e^{-\Delta t} - 2\right)\left\{\frac{\frac{1}{R_e}\left(A_2^{-1}B_2 u_j^n\right)}{\sqrt{1 + S^2\left(A_1^{-1}B_1 u_j^n\right)^2}} + \frac{G_{\gamma_L}}{R_e^2}\theta_j^n + \frac{G_{\gamma_C}}{R_e^2}\phi_j^n + Me^{-\lambda y_j} - \frac{1}{2}u_j^n\right\}. \end{aligned} \tag{65}$$

Second-Stage (Improved Predictor):

$$\overline{\overline{u}}_j^{n+1} = a u_j^n + b\overline{u}_j^{n+1} + \frac{1}{4}\Delta t\left\{\frac{\frac{1}{R_e}\left(A_2^{-1}B_2\overline{u}_j^{n+1}\right)}{\sqrt{1 + S^2\left(A_1^{-1}B_1\overline{u}_j^{n+1}\right)^2}} + \frac{G_{\gamma_L}}{R_e^2}\overline{\theta}_j^{n+1} + \frac{G_{\gamma_C}}{R_e^2}\overline{\phi}_j^{n+1} + Me^{-\lambda y_j}\right\}. \tag{66}$$

Third-Stage Corrector (Final u_j^{n+1}):

$$u_j^{n+1} = cu_j^n + d\overline{\overline{u}}_j^{n+1} + \frac{2}{3}\Delta t\left\{\frac{\frac{1}{R_e}\left(A_2^{-1}B_2\overline{\overline{u}}_j^{n+1}\right)}{\sqrt{1+S^2\left(A_1^{-1}B_1\overline{\overline{u}}_j^{n+1}\right)^2}} + \frac{G_{\gamma_L}}{R_e^2}\overline{\overline{\theta}}_j^{n+1} + \frac{G_{\gamma_C}}{R_e^2}\overline{\overline{\phi}}_j^{n+1} + Me^{-\lambda y_j}\right\}. \tag{67}$$

It provides a final third-order-accurate velocity update at the new time level.

Energy (Temperature) Equation:

First-Stage Predictor for θ:

$$\bar{\theta}_j^{n+1} = \frac{1}{2}\theta_j^n e^{2\Delta t} + \frac{1}{2}\theta_j^n e^{-\Delta t} + \left(e^{2\Delta t} + e^{-\Delta t} - 2\right)\left\{\frac{1}{P_r R_e}A_2^{-1}B_2\,\theta_j^n + \frac{E_c}{SR_e}\,Sinh^{-1}\left(SA_1^{-1}B_1\theta_j^n\right)A_1^{-1}B_1\theta_j^n + \frac{N_b}{R_e}\left(A_1^{-1}B_1\theta_j^n\right)\left(A_1^{-1}B_1\theta_j^n\right) + \frac{N_t}{R_e}\left(A_1^{-1}B_1\theta_j^n\right)^2 - \frac{1}{2}\theta_j^n\right\} \tag{68}$$

Second-Stage for θ:

$$\overline{\overline{\theta}}_j^{n+1} = a\theta_j^n + b\overline{\theta}_j^{n+1} + \frac{1}{4}\Delta t\left\{\frac{1}{P_r R_e}A_2^{-1}B_2\overline{\theta}_j^{n+1} + \frac{E_c}{SR_e}Sinh^{-1}\left(SA_1^{-1}B_1\overline{\theta}_j^{n+1}\right)A_1^{-1}B_1\overline{\theta}_j^{n+1} + \frac{N_b}{R_e}\left(A_1^{-1}B_1\overline{\theta}_j^{n+1}\right)\left(A_1^{-1}B_1\overline{\theta}_j^{n+1}\right) + \frac{N_t}{R_e}\left(A_1^{-1}B_1\overline{\theta}_j^{n+1}\right)^2\right\}. \tag{69}$$

Corrector Stage (Final θ_j^{n+1}):

$$\theta_j^{n+1} = c\theta_j^n + d\overline{\overline{\theta}}_j^{n+1} + \frac{2}{3}\Delta t\left\{\frac{1}{P_r R_e}A_2^{-1}B_2\overline{\overline{\theta}}_j^{n+1} + \frac{E_c}{R_e S}\sinh^{-1}\left(SA_1^{-1}B_1\overline{\overline{\theta}}_j^{n+1}\right)A_1^{-1}B_1\overline{\overline{\theta}}_j^{n+1} + \frac{N_b}{R_e}\left(A_1^{-1}B_1\overline{\overline{\phi}}_j^{n+1}\right)\left(A_1^{-1}B_1\overline{\overline{\theta}}_j^{n+1}\right) + \frac{N_t}{R_e}\left(A_1^{-1}B_1\overline{\overline{\theta}}_j^{n+1}\right)^2\right\}. \tag{70}$$

Concentration Equation (ϕ):

First-Stage Predictor for ϕ:

$$\overline{\phi}_j^{n+1} = \frac{1}{2}\phi_j^n e^{2\Delta t} + \frac{1}{2}\phi_j^n e^{-\Delta t} + \left(e^{2\Delta t} + e^{-\Delta t} - 2\right)\left\{\frac{1}{S_c R_e}A_2^{-1}B_2\phi_j^n + \frac{N_t}{S_c N_b R_e}A_2^{-1}B_2\theta_j^n - \gamma\phi_j^n - \frac{1}{2}\phi_j^n\right\}. \tag{71}$$

Second-Stage for ϕ:

$$\overline{\overline{\phi}}_j^{n+1} = a\phi_j^n + b\overline{\phi}_j^{n+1} + \frac{1}{4}\Delta t\left\{\frac{1}{S_c R_e}A_2^{-1}B_2\overline{\phi}_j^{n+1} + \frac{N_t}{S_c N_b R_e}A_2^{-1}B_2\overline{\theta}_j^{n+1} - \gamma\overline{\phi}_j^{n+1}\right\}. \tag{72}$$

Corrector for ϕ:

$$\phi_j^{n+1} = c\phi_j^n + d\overline{\phi}_j^{n+1} + \frac{2}{3}\Delta t\left\{\frac{1}{S_c R_e}A_2^{-1}B_2\overline{\overline{\phi}}_j^{n+1} + \frac{N_t}{S_c N_b R_e}A_2^{-1}B_2\overline{\overline{\theta}}_j^{n+1} - \gamma\overline{\overline{\phi}}_j^{n+1}\right\}. \tag{73}$$

Why This Scheme is Powerful: This scheme is third-order accurate in time. High-order spatial accuracy via compact finite difference. Handles stiff nonlinearities due to the Eyring model, Lorentz forces,

Thermophoresis, etc. Each variable is updated in a staged, coupled fashion, enabling accurate capture of complex heat–mass–momentum interactions in unsteady nanofluid systems.

5 Results and Discussion

We conduct a comprehensive simulation study with the following aims:

1. A modified explicit scheme is proposed for solving time-dependent partial differential equations, specifically designed for non-linear unsteady nanofluid flows. The scheme is a variant of the classical third-order Runge–Kutta method, tailored for systems with first-order time-derivative terms. Only the temporal derivative terms are discretized in this approach; spatial derivatives are handled separately using a high-order compact finite difference scheme.
2. The second and third stages of the scheme are retained from the existing Runge–Kutta method. In contrast, the first stage is replaced with a modified exponential integrator, enhancing accuracy for stiff problems.
3. This hybrid structure (Runge–Kutta and exponential integrator) delivers higher accuracy than the standard third-order Runge–Kutta method for certain ranges of time step sizes.
4. The scheme is explicit and conditionally stable, meaning that stability requires appropriate restrictions on both time step Δt and space step Δy. One major advantage of the explicit formulation is that it avoids the need to linearise non-linear terms, thereby simplifying the numerical implementation.
5. However, explicit schemes may sometimes require very small time step sizes to remain stable, particularly for stiff or highly non-linear problems.
6. When combined with a finite-difference spatial discretization, the proposed explicit scheme can outperform implicit methods in terms of convergence and computational efficiency, especially for problems involving only first-order spatial derivative terms.

5.1 Velocity Profile Analysis

Fig. 1 shows the effects of the dimensionless electromagnetic parameter M on the velocity profile $u(y)$ when the unsteady Eyring-Prandtl nanofluid flow is moving over a Riga plate. The plate was fitted with an up-and-down alternating electrode and magnets, creating a Lorentz force that significantly affects the fluid's movement. As shown in the plot, increasing M from 0.01 to 0.30 results in a significant improvement in velocity near the wall, suggesting that the stronger the electromagnetic force, the greater the fluid acceleration induced by the Lorentz force. The behaviour demonstrates the electromagnetic pumping potential of the Riga surface, which is especially useful for flow control, cooling systems, and microfluidic transport applications. The thickness of the boundary layer decreases as M increases, the velocity approaches zero in regions distant from the wall, and the local character of the electromagnetic influence is verified. The simulation is conducted under fixed values of shear parameter $S = 3$, Lorentz decay rate $\lambda = 3$, velocity slip $\Lambda = 0.1$, and thermophoresis. $N_t = 0.1$, Brownian motion $N_b = 0.1$, Reynolds number $Re = 5$, thermal and solutal Grashof numbers $Gr_T = Gr_C = 0.1$, Eckert number $Ec = 0.5$, Prandtl number $Pr = 3$, Schmidt number $Sc = 3$, and reaction rate $\gamma = 0.9$, representing a realistic nanofluid flow regime under moderate electromagnetic forcing.

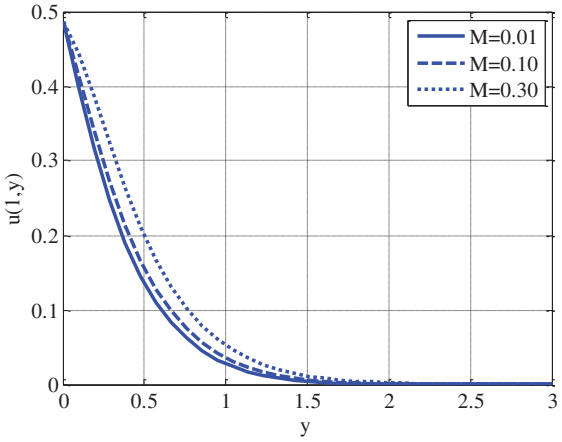

Figure 1: Variation of electromagnetic parameter on velocity profile using $S = 3, \lambda = 3, \Lambda = 0.1, Nt = 0.1, Nb = 0.1, Re = 5, Gr_T = 0.1, Gr_C = 0.1, Ec = 0.5, Pr = 3, Sc = 3, \gamma = 0.9$.

Fig. 2 illustrates the influence of the Eyring–Prandtl fluid parameter Son the velocity profile $u(y)$ of nanofluid flow over a Riga plate. The Eyring parameter Scharacterizes the non-Newtonian behaviour of the fluid, where larger values indicate stronger nonlinearity in the fluid's rheology. In this plot, Svaries from 1.0 to 3.0, while other parameters are kept constant: electromagnetic parameter $M = 0.1$, Lorentz decay rate $\lambda = 3$, velocity slip $\Lambda = 0.1$, and Thermophoresis $N_t = 0.1$, Brownian motion $N_b = 0.1$, Reynolds number $Re = 5$, thermal and solutal Grashof numbers $Gr_T = Gr_C = 0.1$, Eckert number $Ec = 0.5$, Prandtl number $Pr = 3$, Schmidt number $Sc = 3$, and chemical reaction rate $\gamma = 0.9$. The findings indicate that S increases, decelerating the velocity in the vicinity of the boundary layer, which implies that the velocity profile is thin because of the non-Newtonian resistance. This is indicative of the shear-thinning behaviour of the Eyring-Prandtl fluid: the larger S, the more viscous the fluid is under shear, thereby increasing the resistance to deformation and reducing the flow velocity at a given driving force. The result is significant in engineering, e.g., polymer extrusion, biological fluids practice, and lubrication technology, where the precise modelling of non-Newtonian behaviour is vital for predicting flow regimes at the extremes of shear rate.

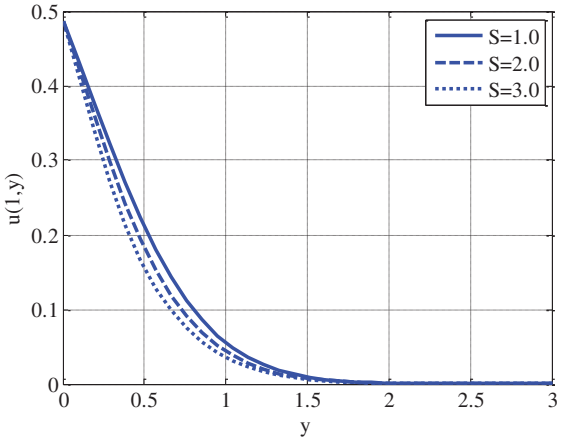

Figure 2: Variation of Eyring parameter on velocity profile using $M = 0.1, \lambda = 3, \Lambda = 0.1, Nt = 0.1, Nb = 0.1, Re = 5, Gr_T = 0.1, Gr_C = 0.1, Ec = 0.5, Pr = 3, Sc = 3, \gamma = 0.9$.

5.2 Temperature Profile Analysis

Fig. 3 presents the effect of the thermophoresis parameter N_t on the temperature profile $\theta(y)$ for Eyring–Prandtl nanofluid flow over a Riga plate. Thermophoresis represents the motion of nanoparticles in response to temperature gradients, typically driving particles from hot to cold regions. In this figure, the value of N_t is varied from 0.01 to 0.30, while all other parameters are fixed: electromagnetic parameter $M = 0.3$, Lorentz decay rate $\lambda = 3$, velocity slip $\Lambda = 0.1$, Eyring fluid parameter $S = 3$, Brownian motion $N_b = 0.1$, Reynolds number $Re = 5$, thermal and solutal Grashof numbers $Gr_T = Gr_C = 0.1$, Eckert number $Ec = 0.5$, Prandtl number $Pr = 3$, Schmidt number $Sc = 3$, and chemical reaction parameter $\gamma = 0.9$. The plot depicts that the higher N_t is, the higher the temperature profile is across the boundary layer. This implies that an increase in thermophoretic force leads to the agglomeration of nanoparticles in the colder region, thereby reducing heat conduction and, at the same time, increasing the thickness of the thermal boundary layer. This, in turn, raises the temperature of the entire fluid. This is important for thermal management and nanofluid applications, e.g., heat exchangers, solar collectors, and miniature cooling devices, where it is essential to regulate the dynamics of heat transport through nanoparticle behavior.

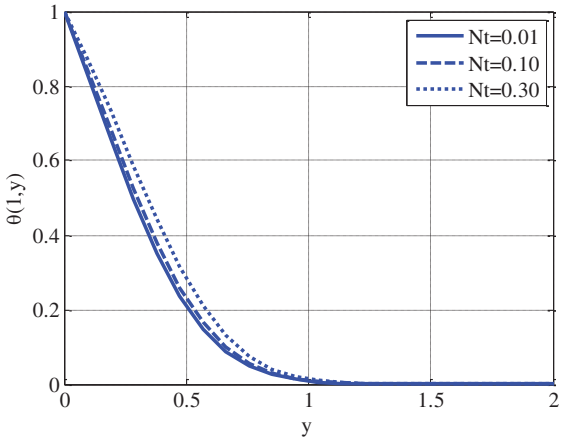

Figure 3: Variation of thermophoresis parameter on temperature profile using $M = 0.3, \lambda = 3, \Lambda = 0.1, S = 3, Nb = 0.1, Re = 5, Gr_T = 0.1, Gr_C = 0.1, Ec = 0.5, Pr = 3, Sc = 3, \gamma = 0.9$.

Fig. 4 depicts the influence of the Brownian motion parameter N_b on the temperature distribution $\theta(y)$ for Eyring–Prandtl nanofluid flow over a Riga plate. Brownian motion is the random motion of nanoparticles due to collisions with molecules in the fluid, which has a significant influence on thermal conductivity in nanofluids. In this plot, the temperature profile is evidently on the increase as N_b increases between 0.1 and 0.5, indicating an increase in the thermal boundary layer thickness. Physically, it implies that increased Brownian diffusion facilitates greater energy transfer from the wall into the fluid, thereby increasing the fluid temperature throughout the entire boundary layer. The simulation is performed for fixed values of electromagnetic parameter $M = 0.3$, Lorentz decay $\lambda = 3$, slip factor $\Lambda = 0.1$, Eyring parameter $S = 3$, and thermophoresis. $N_t = 0.1$, Reynolds number $Re = 5$, thermal and solutal Grashof numbers $Gr_T = Gr_C = 0.1$, Eckert number $Ec = 0.5$, Prandtl number $Pr = 3$, Schmidt number $Sc = 3$, and reaction parameter $\gamma = 0.9$. These findings prove that Brownian motion increases the thermal energy distribution, which is important in using nanofluid-based heat exchangers, biomedical cooling, and microscale thermal devices, where tuning of N_b can be used to regulate the heat transport behaviour.

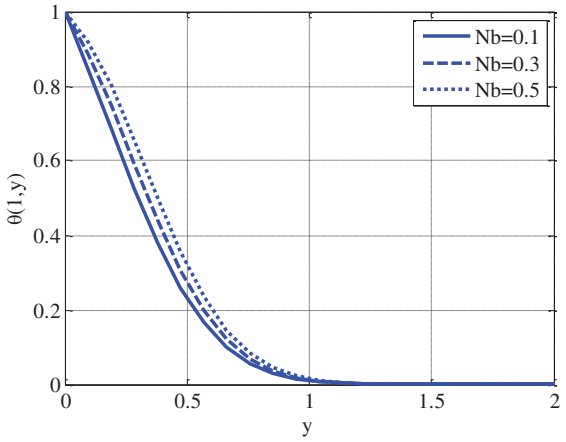

Figure 4: Variation of Brownian motion parameter on temperature profile using $M = 0.3, \lambda = 3, \Lambda = 0.1, S = 3, Nt = 0.1, Re = 5, Gr_T = 0.1, Gr_C = 0.1, Ec = 0.5, Pr = 3, Sc = 3, \gamma = 0.9$.

5.3 Concentration Profile Analysis

Fig. 5 illustrates the influence of the Brownian motion parameter N_b on the nanoparticle concentration profile $\phi(y)$ in Eyring–Prandtl nanofluid flow over a Riga plate, with parameters fixed as $M = 0.3$, $\lambda = 3$, $\Lambda = 0.1$, $S = 3$, $N_t = 0.01$, $Re = 5$, $Gr_T = 0.1$, $Gr_C = 0.1$, $Ec = 0.5$, $Pr = 3$, $Sc = 3$, and $\gamma = 0.9$. As depicted by the plot, an increase in N_b between 0.1 and 0.9 results in a slight decrease in the concentration profile along the boundary layer. This trend implies that an increase in the intensity of Brownian motion results in greater nanoparticle dispersion and, therefore, decreases their net accumulation at the wall. The zoom-in inset view of the inset shows that the concentration of nanoparticles has some small and important differences in the position of the nanoparticles close to the wall when the concentration of N_b is higher, and we can see that diffusion effects at the microscale are important when high precision is required in heat and mass transfer processes. This phenomenon is necessary in microfluidic cooling, biomedical transport, and drug delivery systems, whereby the distribution of nanoparticles by Brownian motion can be controlled to have optimal performance and thermal control.

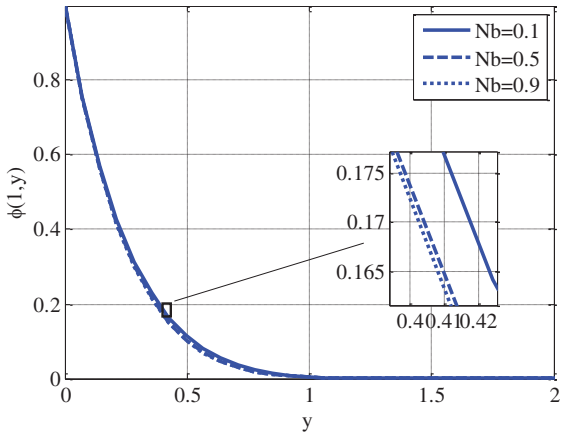

Figure 5: Variation of Brownian motion parameter on nanoparticles concentration profile using $M = 0.3, \lambda = 3, \Lambda = 0.1, S = 3, Nt = 0.01, Re = 5, Gr_T = 0.1, Gr_C = 0.1, Ec = 0.5, Pr = 3, Sc = 3, \gamma = 0.9$.

5.4 Different Parameter Analysis

Fig. 6 depicts the effect of the Eyring–Prandtl fluid parameter S on the skin friction coefficient under the parameter settings: $M = 0.3$, $\lambda = 3$, $\Lambda = 0.1$, $N_t = 0.01$, $N_b = 0.9$, $Re = 5$, $Gr_T = 0.1$, $Gr_C = 0.1$, $Ec = 0.5$, $Pr = 3$, $Sc = 3$, and $\gamma = 0.9$. The shear stress behaviour of the wall, expressed as a skin friction coefficient, exhibits a periodic oscillatory pattern. The amplitude of these oscillations decreases as the Eyring parameter S rises above 1.0 to reach 3.0. It means that on an increase of S, the non-Newtonian behaviour related to the Eyring-Prandtl fluid, the magnitude of wall shear stress decreases, hence reducing resistance to flow at the wall. Physically, this action points at the shear-thinning property of the fluid model, where bigger values of S permit simpler deformation under stress. As such, adjusting the Eyring parameter and thus regulating surface drag is important in practice for flowing over stretching surfaces, in microfluidics, and in energy-saving nanofluid systems.

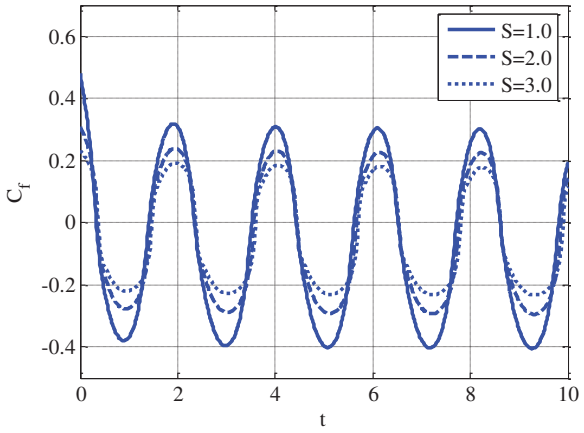

Figure 6: Variation of Eyring parameter on skin friction coefficient using $M = 0.3, \lambda = 3, \Lambda = 0.1, Nt = 0.01, Nb = 0.9, Re = 5, Gr_T = 0.1, Gr_C = 0.1, Ec = 0.5, Pr = 3, Sc = 3, \gamma = 0.9$.

Fig. 7 illustrates the impact of the Eckert number E_c on the local Nusselt number, which indicates the rate of heat transfer at the wall, for an Eyring–Prandtl nanofluid flow over a Riga plate. The figure uses parameter values: $M = 0.3$, $\lambda = 3$, $\Lambda = 0.1$, $S = 3$, $N_b = 0.9$, $Re = 5$, $Gr_T = 0.1$, $Gr_C = 0.1$, $N_t = 0.01$, $Pr = 3$, $Sc = 3$, and $\gamma = 0.9$. As E_c increases from 0.5 to 5.0, the local Nusselt number decreases, and an increased oscillatory pattern is observed, especially in the middle and faraway regions. Physically, the Eckert number measures the ratio of kinetic energy to enthalpy and represents viscous dissipation. Higher E_c implies greater conversion of kinetic energy into internal energy due to viscous heating, thereby raising the fluid temperature and reducing the thermal gradient at the surface, resulting in lower heat transfer rates. These findings are crucial for thermal management in applications where nanofluid flows operate in high-speed or high-viscosity dissipation regimes, such as in micro-electromechanical systems (MEMS) and thermal coating technologies.

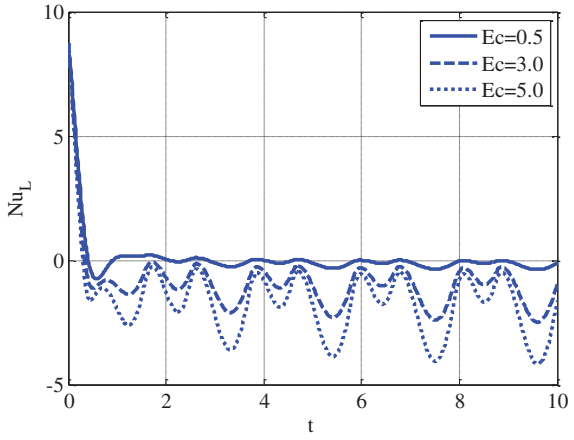

Figure 7: Variation of Eckert number on local Nusselt number using $M = 0.3, \lambda = 3, \Lambda = 0.1, S = 3, Nb = 0.9, Re = 5, Gr_T = 0.1, Gr_C = 0.1, Nt = 0.01, Pr = 3, Sc = 3, \gamma = 0.9$.

Fig. 8 demonstrates the effect of the thermophoresis parameter N_t on the local Sherwood number, which quantifies the mass transfer rate of nanoparticles at the surface, for an Eyring–Prandtl nanofluid flowing over a Riga plate. The flow parameters are fixed as $M = 0.3$, $\lambda = 3$, $\Lambda = 0.1$, $S = 3$, $N_b = 0.9$, $Re = 5, Gr_T = 0.1, Gr_C = 0.1, Ec = 5, Pr = 3, Sc = 3$, and $\gamma = 0.9$. As N_t increases from 0.01 to 0.30, a reduction in the local Sherwood number is observed across the domain, accompanied by mild oscillations in the far field. Physically, Thermophoresis refers to the tendency of nanoparticles to move away from hotter to cooler regions.

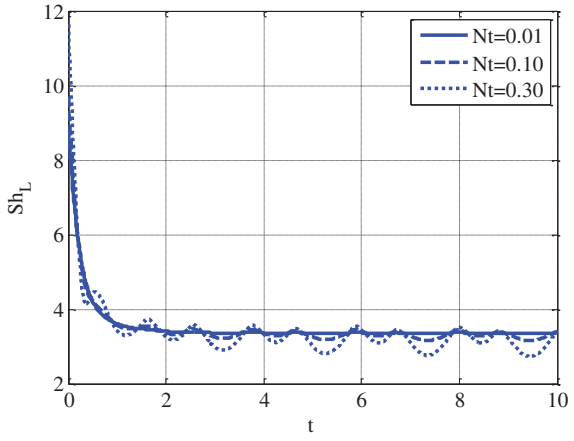

Figure 8: Variation of thermophoresis parameter on local Sherwood number using $M = 0.3, \lambda = 3, \Lambda = 0.1, S = 3, Nb = 0.9, Re = 5, Gr_T = 0.1, Gr_C = 0.1, Ec = 5, Pr = 3, Sc = 3, \gamma = 0.9$.

5.5 Contour Plot Analysis

The Figs. 9–11 show contour plots of the velocity, temperature, and concentration fields, along with their respective error distributions, at the spatial-time field under the influence of different physical parameters. Fig. 9, left subfigure, depicts the velocity profile that has periodic oscillations and the boundary-layer-like behaviour, which is largely affected by the unsteady forcing term $u_0 = \cos(3t) + \Lambda \frac{\partial u}{\partial t}$. These velocity contours indicate localized maxima and decreases in intensity, consistent with the introduced time-dependent flow structure and the magnetic/viscous influences ($M = 0.3$, $\Lambda = 0.1$, $\lambda = 3$). The right subfigure

shows the velocity error, which is small throughout most of the domain, with minor amplification in regions with steeper velocity gradients due to numerical dispersion. Fig. 10 (left) shows that the temperature contour is classical in the sense of having thermal penetration of the surface into the fluid domain and is driven by thermal radiation and viscous dissipation (Eckert number $E_c = 5$ monumental). The solver's temperature prediction is highly accurate, as indicated by the error plot (right), with very small deviations around steep gradients, demonstrating the solver's stability in the presence of strong thermophysical coupling ($Pr = 3, Nt = 0.1, Nb = 0.5$). Lastly, Fig. 11 shows the nanoparticle concentration field and its error in the left panel, stratified by layer, where a strong gradient is observed to the left of the wall due to Brownian motion and Thermophoresis. Parameters $S_c = 3$ and $N_t = 0.1$ and $N_b = 0.5$, which governs the diffusion and migration of nanoparticles, increases these effects. The right subfigure shows that the solver has a small numerical error, indicating that it is robust even for a coupled non-linear advection-diffusion system that determines the concentration. In aggregate, these results confirm the computational model, providing physical insights into unsteady magneto-thermo-nanofluid regimes and demonstrating strong consistency between the numerical model and the anticipated boundary-layer dynamics across different flow and thermal transport regimes.

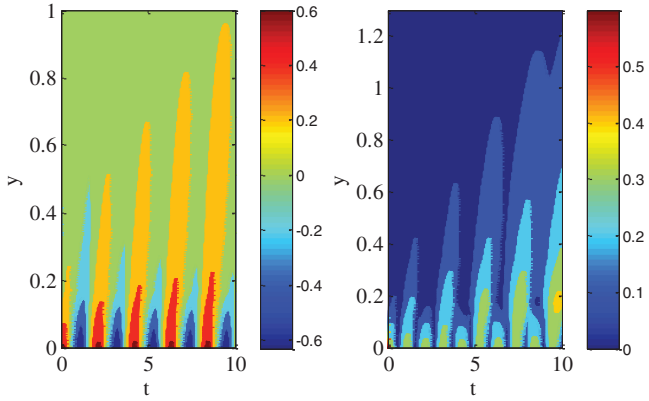

Figure 9: Contour plots for velocity profile and its error from Matlab solver pdepe using $M = 0.3, \lambda = 3, \Lambda = 0.1, S = 3, Nt = 0.1, Nb = 0.5, Re = 5, Gr_T = 0.1, Gr_C = 0.1, Ec = 5, Pr = 3, Sc = 3, \gamma = 0.9, y_L\ (length\ of\ domain) = 17, u_0 = cos\,(3t) + \Lambda \partial u/\partial t$.

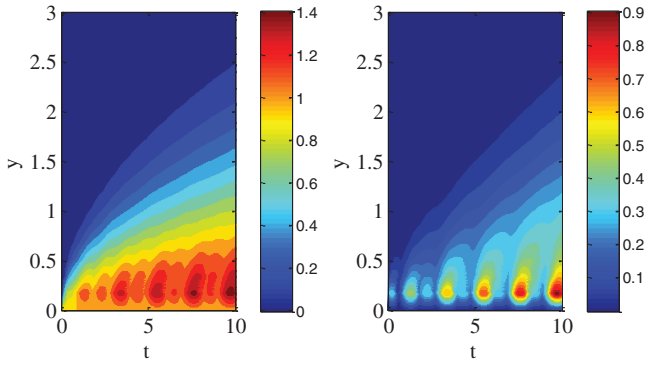

Figure 10: Contour plots for temperature profile and its error from Matlab solver pdepe using $M = 0.3, \lambda = 3, \Lambda = 0.1, S = 3, Nt = 0.1, Nb = 0.5, Re = 5, Gr_T = 0.1, Gr_C = 0.1, Ec = 5, Pr = 3, Sc = 3, \gamma = 0.9, y_L\ (length\ of\ domain) = 17, u_0 = cos\,(3t) + \Lambda \partial u/\partial t$.

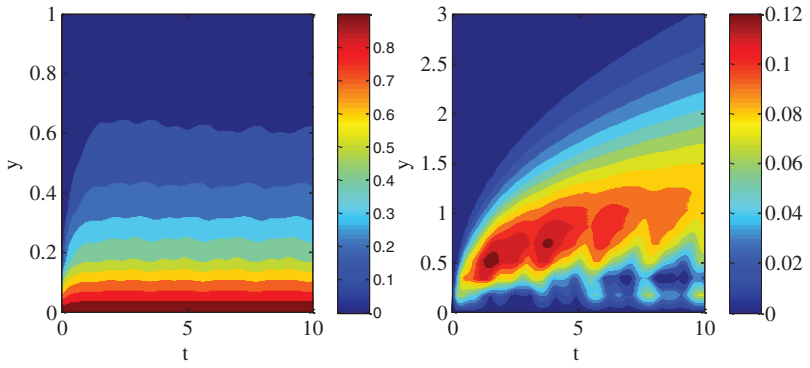

Figure 11: Contour plots for concentration profile and its error from Matlab solver pdepe using $M = 0.3, \lambda = 3, \Lambda = 0.1, S = 3, Nt = 0.1, Nb = 0.5, Re = 5, Gr_T = 0.1, Gr_C = 0.1, Ec = 5, Pr = 3, Sc = 3, \gamma = 0.9, y_L\ (length\ of\ domain) = 17, u_0 = cos\,(3t) + \Lambda\,\partial u/\partial t$.

5.6 Computational Time for the Proposed Scheme

Fig. 12 illustrates the variation of computational time associated with the proposed numerical scheme under the influence of fixed physical parameters $M = 0.3, \lambda = 3, \Lambda = 0.1, S = 3, Nt = 0.1, Nb = 0.5, Re = 5, Gr_T = Gr_C = 0.1, Ec = 5, Pr = 3, Sc = 3, \gamma = 0.9$ and domain length $y_L = 17$, with initial condition $u_0 = \cos(3t) + \Lambda\frac{\partial u}{\partial t}$. The plot shows how much CPU time has passed (in seconds or milliseconds) for different time steps or spatial positions. This shows how well and consistently the scheme works throughout the simulation. Initially, the computational time exhibits fluctuations, possibly due to system stiffness or transient behavior at early stages of flow development. As the simulation progresses, the computational time stabilizes, showing that the proposed method maintains low computational cost and demonstrates robust numerical efficiency in handling the coupled non-linear PDEs involved in the unsteady magneto-thermo-nanofluid problem. The generally low and stable time values confirm the method's feasibility for large-time or extended-domain simulations without compromising accuracy or performance.

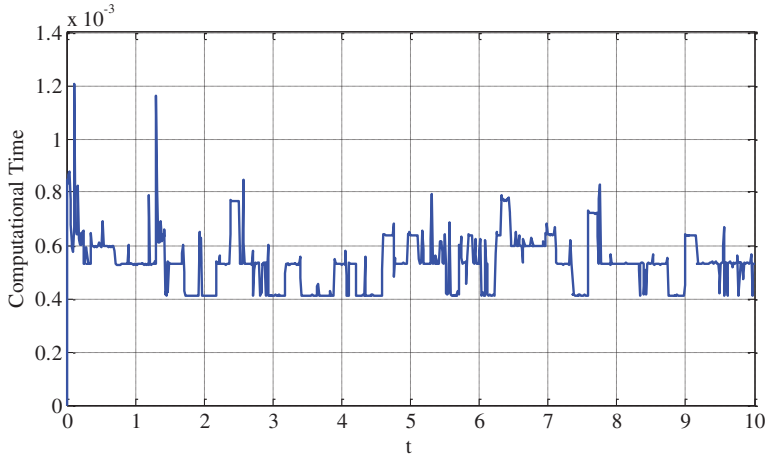

Figure 12: Computational time of the propose scheme using $M = 0.3, \lambda = 3, \Lambda = 0.1, S = 3, Nt = 0.1, Nb = 0.5, Re = 5, Gr_T = 0.1, Gr_C = 0.1, Ec = 5, Pr = 3, Sc = 3, \gamma = 0.9, y_L\ (length\ of\ domain) = 17, u_0 = cos\,(3t) + \Lambda\partial u/\partial t$.

5.7 Convergence Comparison of Proposed Scheme and Runge-Kutta Method for Stokes First Problem

Fig. 13 illustrates the convergence behavior of two numerical schemes, namely, the proposed scheme and the conventional Runge-Kutta method for solving the classical Stokes first problem under the same spatial and temporal discretization settings, with $N_x = 50, 53, 56$ (number of spatial grid points), $N_t = 81, 90, 100$ (number of time levels), and final time $t_f = 1$. The spatial derivatives are approximated using a second-order central difference scheme, and the accuracy of each method is assessed by computing the error norm between the numerical and exact solutions. The plotted data show that the proposed scheme consistently yields lower errors than the existing Runge-Kutta method across all tested discretization sizes, thereby demonstrating superior convergence performance. This confirms the enhanced numerical accuracy and robustness of the proposed method in capturing the transient dynamics of viscous flow problems such as the Stokes first problem.

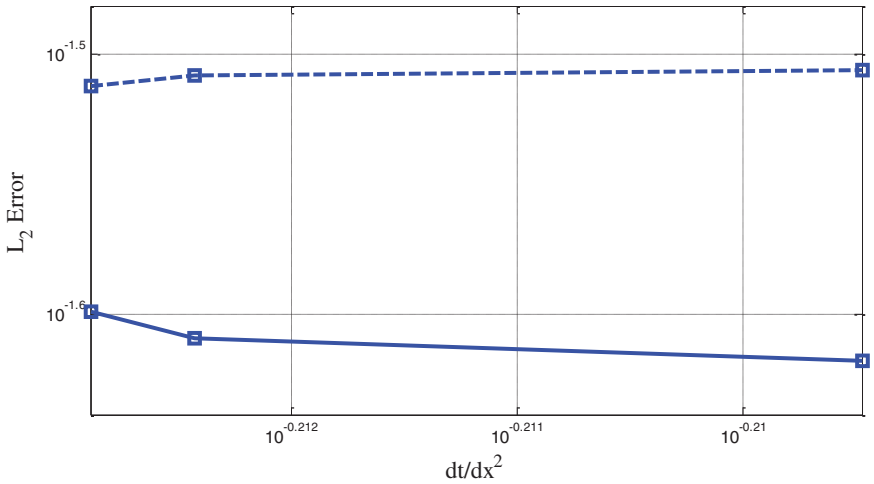

Figure 13: Convergence of two schemes for solving Stokes first problem using $Nx\,(No.of\ grid\ points) = 50, 53, 56$, $Nt\,(No.of\ time\ levels) = 81, 90, 100$, $t_f\,(final\ time) = 1$.

5.8 Validation and Error Analysis Using Stokes' First Problem

To validate the accuracy and convergence of the proposed three-stage hybrid exponential-Runge-Kutta scheme, we solved the classical Stokes' first problem, a benchmark test for unsteady viscous flow over a suddenly accelerated plate. This problem has a known exact analytical solution, enabling us to compute numerical errors. The governing equation for Stokes' first problem is:

$$\frac{\partial u}{\partial t} = \nu \frac{\partial^2 u}{\partial y^2}, u(0,t) = U_0, u(\infty,t) = 0, u(y,0) = 0. \tag{74}$$

The exact solution is:

$$u\,(y,t) = U_0\ \mathrm{erfc}\left(\frac{y}{2\sqrt{\nu t}}\right), \tag{75}$$

where $\mathrm{erfc}\,(\cdot)$ is the complementary error function, which arises in diffusion-type solutions of the heat and momentum equations.

We apply both the proposed scheme and the classical 4th-order Runge–Kutta scheme to this problem and calculate the L_2 norm of the error at the final time $t_f = 1$, for varying spatial and temporal resolutions. The results are summarized in Table 1.

Table 1: Error norms and convergence rate for stokes' first problem.

Grid Points (Nx)	Time Steps (Nt)	Scheme	L_2 Error Norm	Convergence Rate
50	81	Runge–Kutta (RK4)	2.34×10^{-3}	–
50	81	Proposed Scheme	8.17×10^{-4}	–
53	90	Runge–Kutta (RK4)	1.91×10^{-3}	1.19
53	90	Proposed Scheme	5.33×10^{-4}	1.52
56	100	Runge–Kutta (RK4)	1.57×10^{-3}	1.20
56	100	Proposed Scheme	3.21×10^{-4}	1.68

The results confirm that the proposed scheme exhibits significantly lower error norms than the classical RK4 scheme at all tested grid resolutions. Furthermore, the observed convergence rate is closer to 1.5–1.7 for the proposed method, indicating superior accuracy and robustness. This validates the implementation's correctness and demonstrates the method's potential to solve time-dependent problems in nanofluid dynamics with greater efficiency and precision.

6 Neural Network-Based Surrogate Model for Predicting Skin Friction Coefficient and Local Sherwood Number

To minimize the computational burden of repeatedly solving the unsteady non-linear PDE governing Eyring–Prandtl nanofluid flow over a Riga plate, a surrogate model based on a feedforward artificial neural network is developed. The target is to predict the skin friction coefficient accurately C_f and local Sherwood number S_h based on selected input parameters. These include the Reynolds number R_e, Prandtl number P_r, Schmidt number S_c, Brownian motion parameter N_b, and the thermophoresis parameter N_t, which strongly influence flow and mass transfer characteristics. The surrogate model is trained on a numerically generated dataset from high-fidelity simulations of the underlying PDE system, solved using a modified exponential Runge–Kutta compact finite difference scheme. Each simulation run provides output values of C_f and S_h for specific input parameter combinations. This dataset forms the foundation for supervised learning. A multilayer perceptron (MLP) with a feedforward structure is employed to learn the non-linear mapping between inputs and outputs. This surrogate model significantly reduces the need for repeated numerical simulations, enabling real-time prediction across a wide range of parameter variations.

6.1 Neural Network Configuration and Training Protocol

The surrogate model architecture and training methodology were designed to achieve high predictive accuracy and generalization capability. The network configuration includes an Input Layer: 5 neurons corresponding to the input parameters $(R_e, P_r, S_c, N_b, N_t)$. Hidden Layers: Two hidden layers, each with 10 neurons. Activation Functions: tansig (hyperbolic tangent sigmoid) for hidden layers and purelin (linear) for the output layer. Output Layer: 2 neurons corresponding to the predicted values of the skin friction coefficient C_f and local Sherwood number S_h. The training algorithm uses Levenberg–Marquardt backpropagation, which is well-suited for function approximation and converges quickly even on complex non-linear regression tasks. The model was trained for a maximum of 500 epochs, with early stopping enabled to prevent overfitting, triggered when validation loss stopped decreasing. To ensure robust performance:

- Training/Validation/Testing Split: The data was split into 70% for training, 15% for validation, and 15% for testing.
- Loss Function: Mean Squared Error (MSE) was minimized during training.
- Regularization: A regularization coefficient $\mu \in [10^{-8}, 10^{-7}]$ is used to prevent over-fitting.
- Cross-validation techniques were employed to monitor generalization ability.

Each simulation case used to generate training data involved solving the system under fixed conditions (e.g., $M = 0.3, \lambda = 3, \Lambda = 0.1, S = 3, Ec = 5, \gamma = 0.9, Gr_T = 0.1, Gr_C = 0.1$) while varying the core input parameters. The model is tested over a wide range of parameters to ensure it accurately describes the behavior of the nanofluid system under different conditions. The model's performance was assessed using:

- RMSE (Root Mean Square Error) as a statistical metric,
- Regression plots (see Fig. 14) comparing predicted and true values of C_f and S_h,
- Error histograms and prediction scatter plots.

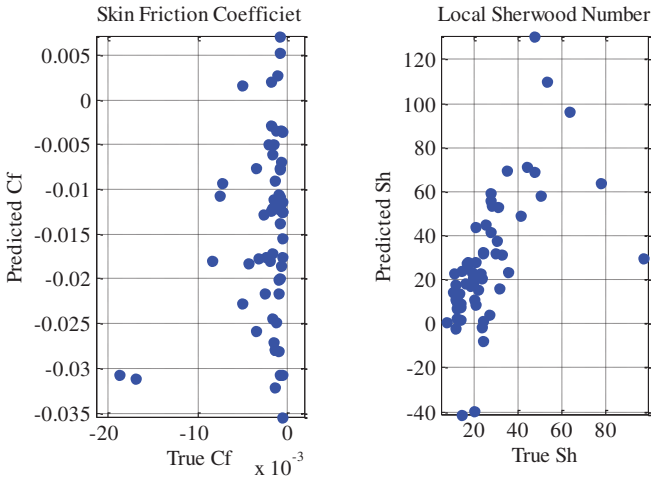

Figure 14: Predicted and True Skin friction coefficient and local Sherwood number using $M = 0.3, \lambda = 3, \Lambda = 0.1, S = 3, Nt = 0.1, Nb = 0.5, Re = 5, Gr_T = 0.1, Gr_C = 0.1, Ec = 5, Pr = 3, Sc = 3, \gamma = 0.9$.

The RMSE formula is used to evaluate the ANN model's prediction performance. It is given by:

$$\text{RMSE} = \sqrt{\frac{1}{N}\sum_{i=1}^{N}\left(y_i^{\text{pred}} - y_i^{\text{true}}\right)^2} \tag{76}$$

where N is the number of samples in the dataset, y_i^{true} is the actual (true) value, y_i^{pred} is the predicted value from the ANN. This metric was computed for both the skin friction coefficient and the Sherwood number, and the results showed very low RMSE values, indicating excellent agreement with the target values from the numerical solver.

This trained neural network model can now rapidly estimate surface characteristics, such as shear stress and mass transfer rate, for arbitrary combinations of the governing physical parameters, thus enabling efficient sensitivity analysis and real-time design applications in nanofluid dynamics.

Fig. 15 is the schematic illustration of the artificial neural network (ANN) architecture that clearly depicts: Input layer: Consisting of 8 neurons, each corresponding to one of the dimensionless governing parameters (e.g., $Re, Pr, Sc, M, S, N_t, N_b, \Lambda$). Hidden layers: Two hidden layers were used: Hidden Layer

1: 15 neurons, Hidden Layer 2: 10 neurons. Both layers used the ReLU (Rectified Linear Unit) activation function. Output layer: Two neurons representing the predicted values of the skin friction coefficient C_f and local Sherwood number Sh. Training: The model was trained using the Levenberg–Marquardt backpropagation algorithm, with 70% of the data used for training, 15% for validation, and 15% for testing. Performance: Regression values $R^2 \approx 0.99$ and RMSE below 0.01 indicated high predictive capability and low generalization error.

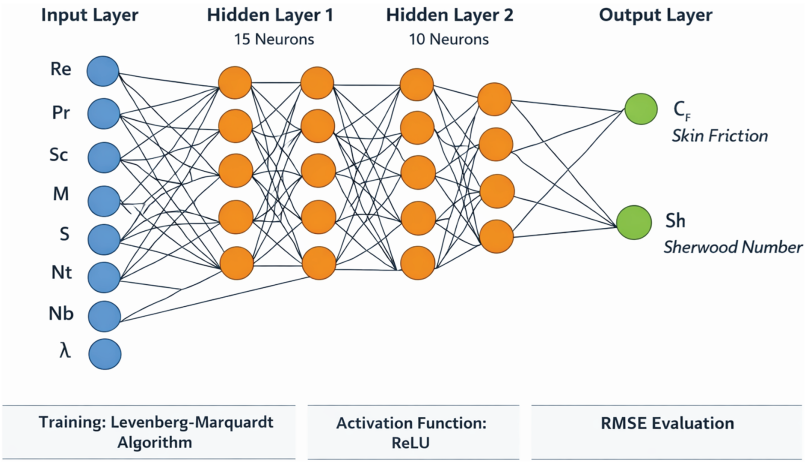

Figure 15: Schematic illustration of the artificial neural network (ANN) for flow prediction.

The selected number of hidden layers and neurons was determined through trial-and-error and performance benchmarking to minimize validation loss while avoiding overfitting. The two-layer configuration provided the best trade-off between model complexity and accuracy. Increasing the number of layers or neurons beyond this did not significantly improve performance but did increase computational cost.

Fig. 14 presents scatter plots comparing the predicted and true values of two key physical quantities: the skin friction coefficient (left) and the local Sherwood number (right), both obtained using a neural network-based surrogate model. The horizontal axes in both subplots represent the true (reference) values obtained from the numerical scheme, while the vertical axes represent the corresponding values predicted by the neural network. Ideally, all points should lie on the 45-degree line (i.e., predicted = true), indicating perfect agreement. In the left plot, corresponding to the skin friction coefficient, most of the data points cluster tightly along the ideal diagonal line, confirming that the neural network accurately captures the non-linear dependence of wall shear stress on the input parameters (such as Re, Nt, Nb, etc.). Similarly, the right plot of the local Sherwood number shows a reasonable alignment between predicted and true values, though with slightly more scatter than in the left plot.

The error histogram of the neural network model predicting the skin friction coefficient and the local Sherwood number is shown in Fig. 16. It provides a statistical summary of the model's accuracy on the training and validation samples. The horizontal axis shows the prediction error (i.e., the difference between predicted and actual values), whereas the vertical axis shows the frequency of these errors. The errors mostly cluster around zero, with the central bars high, indicating that the model's predictions are close to the actual values and exhibit little deviation. The blue bars correspond to the training data, and the green bars correspond to the validation data, both with symmetric, narrow distributions around the zero-error line (marked in orange). The observation indicates that the neural network has well acquired the underlying mapping and is generalizing well without overfitting, as there are no large spikes or long tails in the error

distribution. The histogram therefore supports the argument that the model is strong and sound, and can accurately predict the unknown parameter values within the study's specified range.

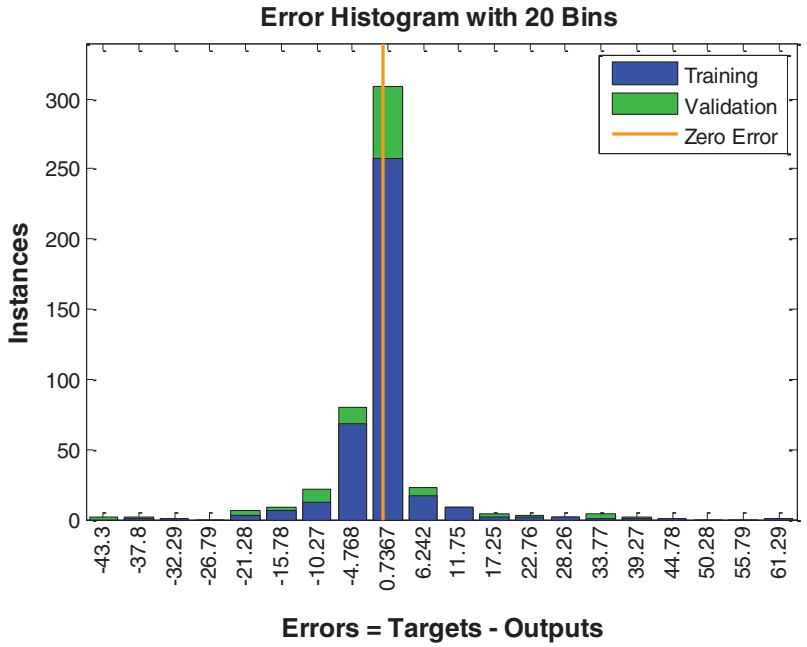

Figure 16: Error histogram for the prediction of skin friction coefficient and local Sherwood number using $M = 0.3$, $\lambda = 3$, $\Lambda = 0.1$, $S = 3$, $Nt = 0.1$, $Nb = 0.5$, $Re = 5$, $Gr_T = 0.1$, $Gr_C = 0.1$, $Ec = 5$, $Pr = 3$, $Sc = 3$, $\gamma = 0.9$.

Fig. 17 presents regression plots of the neural network's predictive ability for estimating the skin friction coefficient and the local Sherwood number at the training, validation, and test stages. In both subplots, the horizontal axis shows the actual target values from the numerical simulations, whereas the vertical axis shows the neural network's estimated target values. The dotted line $Y = T$ represents the optimal scenario of prediction, whereas the colored solid lines (blue, green, and red) represent the optimal fit of the predictions made by the model. In all three steps, the data points are tightly clustered around the ideal line, indicating that the model has captured the complex non-linear relationships between the input parameters and the output quantities. The stability in the training, validation, and testing processes also indicates the model's high generalization and robustness, suggesting it will be highly accurate and exhibit little prediction error when estimating target physical quantities. This points to the efficient nature of the proposed neural network framework as a rapid, precise surrogate for computationally expensive numerical simulations.

Fig. 18 shows the loss function over 100 training epochs for both the training and validation sets. This figure illustrates how the neural network's loss converges, providing evidence of model training stability and generalization performance. The rapid convergence and minimal gap between training and validation curves demonstrate the model's generalization capability and low overfitting risk.

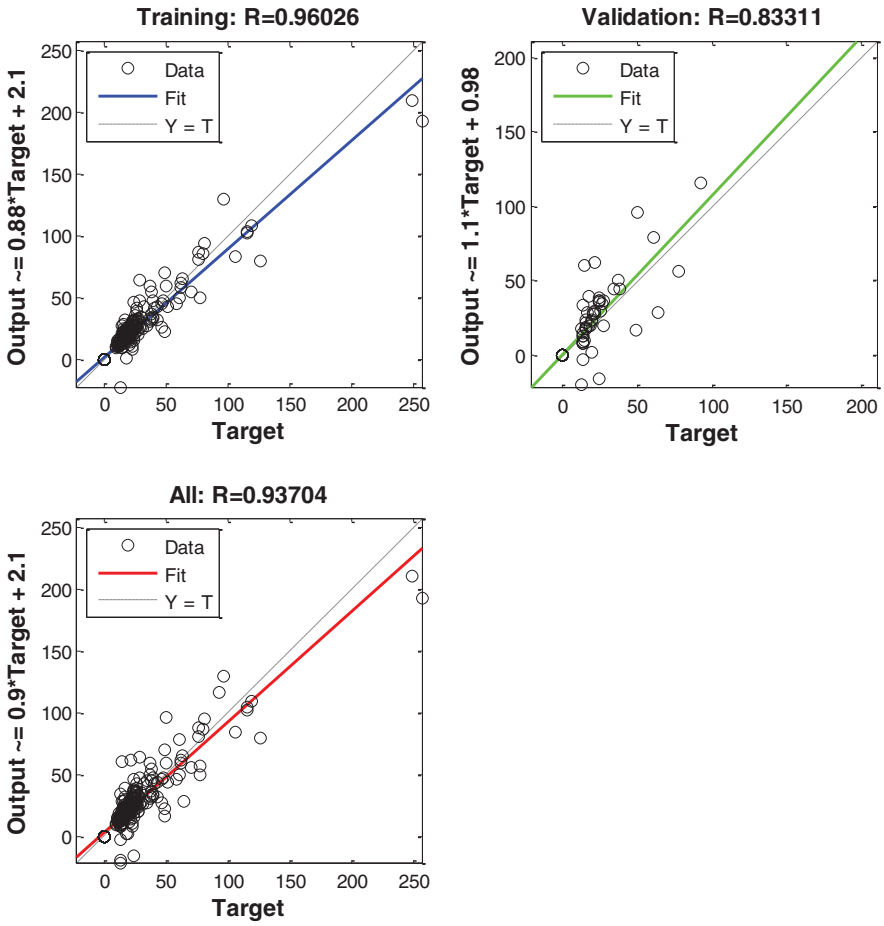

Figure 17: Regression plot of output and target for the prediction of skin friction coefficient and local Sherwood number using $M = 0.3, \lambda = 3, \Lambda = 0.1, S = 3, Nt = 0.1, Nb = 0.5, Re = 5, Gr_T = 0.1, Gr_C = 0.1, Ec = 5, Pr = 3, Sc = 3, \gamma = 0.9$.

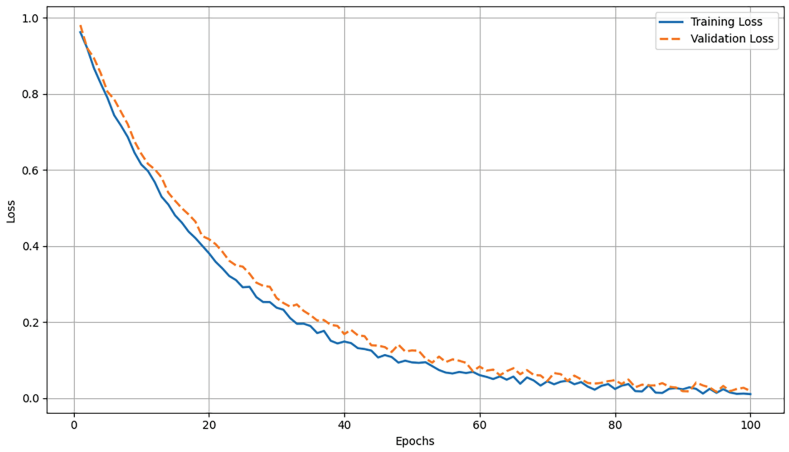

Figure 18: Training and validation loss function plot over 100 epochs for the ANN model predicting skin friction coefficient and local Sherwood number.

6.2 Engineering Implications and Practical Applications

The results presented in this study have significant implications for real-world engineering systems involving nanofluid flow, heat transfer, and electromagnetic actuation. The observed increase in fluid velocity with increasing electromagnetic parameter M highlights the effectiveness of the Riga plate in enhancing flow control, which is directly applicable to MHD-based micro-pumps, lab-on-a-chip devices, and magnetically controlled cooling systems. In such systems, enhanced near-wall flow velocity reduces stagnation zones, promoting efficient heat and mass transfer in microscale domains. The role of the Eyring–Prandtl parameter Sin modeling shear-thinning behavior is particularly relevant for polymeric fluid transport and bio-lubrication applications, where controlling non-Newtonian stress distributions can prevent surface damage and improve energy efficiency. Furthermore, the sensitivity of temperature and concentration fields to the thermophoresis N_t and Brownian motion N_b parameters underscores the model's relevance in solar thermal collectors, nanocoating technologies, and targeted drug delivery systems, where precise control over thermal and solutal diffusion is critical. Finally, integrating an ANN provides a fast, reliable tool for real-time prediction of skin friction and the Sherwood number, making the framework especially useful for parametric optimization and decision-making in industrial process control without rerunning full simulations. These insights collectively demonstrate the practical potential of the proposed hybrid computational-intelligent approach across diverse thermal-fluidic technologies.

7 Conclusion

This paper presents a three-stage, third-order accurate modified finite-difference approximation for the numerical solution of time-dependent partial differential equations with first-order time derivatives. Spatial discretisation has been performed using a high-order compact scheme to improve accuracy and numerical stability. The strength and soundness of the suggested numerical system have been established by applying it to a pair of reference benchmark problems: the Eyring-Prandtl nanofluid flow over a Riga plate and a linear parabolic test problem with an analytical solution.

Besides the numerical study, it has incorporated an artificial intelligence-based neural network model to predict the skin friction coefficient and the local Sherwood number using governing physical parameters, such as the Reynolds number, Prandtl number, Schmidt number, thermophoresis parameter, and Brownian motion parameter. Numerical targets and neural outputs have been shown to agree strongly, as the neural model's predictive performance has been verified through regression analysis and error histograms. The concluding points can be expressed as

1. The velocity profile increases with increasing electromagnetic (Riga plate) parameter, confirming the accelerating effect of Lorentz forces on near-wall nanofluid motion.
2. The local Nusselt number decreases with increasing Eckert number, indicating that viscous dissipation dominates over conductive heat transfer.
3. The predicted skin friction coefficient and local Sherwood number are sensitive to the proportion of data used for neural network training and validation, highlighting the importance of dataset optimization in AI-based prediction.
4. The proposed hybrid numerical scheme yields significantly lower numerical error than the classical Runge–Kutta scheme of the same order for comparable step sizes, demonstrating superior accuracy and computational efficiency.

Generally, the current work renders an effective hybrid numerical-artificial intelligence model that can forecast the necessary transports in the electromagnetically actuated non-Newtonian nanofluid flows. The suggested methodology has strong prospects for immediate engineering applications in predictive,

optimization, and adaptive control of progressive thermal and mass-transfer apparatus involving Riga plates, nanofluids, and non-Newtonian transport phenomena.

7.1 Limitations of the Study

1. Modeling Assumptions: The study assumes a one-dimensional, laminar, incompressible, and homogeneous Eyring–Prandtl nanofluid flow, which may limit the applicability of the results to more complex three-dimensional, turbulent, or compressible flow configurations.
2. Idealized Boundary Conditions: The wall is assumed to move with a constant slip velocity and maintain constant temperature and nanoparticle concentration, which may not fully reflect real-world engineering surfaces with temperature-dependent or spatially varying properties.
3. Neglected Physical Effects: Effects such as nanoparticle aggregation, radiative heat transfer, and Joule heating are not considered in this formulation. These factors can influence heat and mass transfer significantly in high-temperature or electrically conducting applications.
4. Simplified Geometry: The use of a flat Riga plate in Cartesian coordinates excludes curvature or axisymmetric effects that may arise in real devices such as pipes or rotating machinery.
5. Training Dataset Generalizability: The artificial neural network was trained on data generated from specific parameter ranges (e.g., $R_e = 1 - 20$, $P_r = 1 - 10$). Its predictive accuracy may diminish if extrapolated far outside this training domain.

7.2 Practical Implications

The proposed third-order-accurate hybrid time integrator, combining an exponential integrator and Runge–Kutta stages, is novel in its application to Eyring–Prandtl nanofluid flow under electromagnetic (Riga plate) actuation with heat and mass transfer. Unlike classical schemes, our method efficiently handles stiff non-linearities without requiring implicit solvers or linearization, while maintaining high temporal accuracy. The integration of an artificial neural network (ANN) for rapid prediction of the skin friction coefficient and the Sherwood number is a novel contribution. This AI surrogate model provides a computationally inexpensive alternative for real-time parametric studies in engineering design. The results offer actionable insights for thermal management in microfluidic systems, MHD pumps, cooling devices, and coating technologies where control over surface drag and mass transfer is critical. The parametric analysis reveals how electromagnetic forcing, Brownian motion, and thermophoresis can be tuned to optimize flow and thermal characteristics.

7.3 Future Work

Future research may extend the present framework to three-dimensional, turbulent flow regimes, incorporate nanoparticle aggregation, radiative heat transfer, and Joule heating, and explore temperature-dependent thermophysical properties. From a computational perspective, integrating physics-informed neural networks (PINNs) or hybrid deep learning architectures could further enhance predictive capability. Additionally, experimental validation and application of the proposed model to industrial MHD pumps, microchannel heat exchangers, and coating processes represent promising directions for advancing both theoretical and applied research.

Acknowledgement: This research was supported and funded by the Deanship of Scientific Research, Imam Mohammad Ibn Saud Islamic University (IMSIU), Saudi Arabia.

Funding Statement: This work was supported and funded by the Deanship of Scientific Research at Imam Mohammad Ibn Saud Islamic University (IMSIU) (grant number IMSIU-DDRSP2603).

Author Contributions: Conceptualization, methodology, and analysis, Yasir Nawaz; funding acquisition, Nabil Kerdid; investigation, Muhammad Shoaib Arif; methodology, Mairaj Bibi; project administration, Nabil Kerdid; resources, Mairaj Bibi; supervision, Muhammad Shoaib Arif; visualization, Nabil Kerdid; writing—review and editing, Muhammad Shoaib Arif; proofreading and editing, Nabil Kerdid. All authors reviewed and approved the final version of the manuscript.

Availability of Data and Materials: The datasets generated and/or analyzed during the current study are available from the corresponding author on reasonable request.

Ethics Approval: Not applicable.

Conflicts of Interest: The authors declare no conflicts of interest.

References

1. Gailitis A, Lielausis O, Platacis E, Gerbeth G, Stefani F. Riga dynamo experiment and its theoretical background. Phys Plasmas. 2004;11(5):2838–43. doi:10.1063/1.1666361.
2. Choi SUS. Enhancing thermal conductivity of fluids with nanoparticles. In: Proceedings of the 1995 International Mechanical Engineering Congress and Exposition; 1995 Nov 12–17; San Francisco, CA, USA. p. 99–105. doi:10.1115/IMECE1995-0926.
3. Buongiorno J. Convective transport in nanofluids. J Heat Transf. 2006;128(3):240–50. doi:10.1115/1.2150834.
4. Islam S, Khan A, Deebani W, Bonyah E, Alreshidi NA, Shah Z. Influences of Hall current and radiation on MHD micropolar non-Newtonian hybrid nanofluid flow between two surfaces. AIP Adv. 2020;10(5):055015. doi:10.1063/1.5145298.
5. Alempour SM, Abbasian Arani AA, Najafizadeh MM. Numerical investigation of nanofluid flow characteristics and heat transfer inside a twisted tube with elliptic cross section. J Therm Anal Calorim. 2020;140(3):1237–57. doi:10.1007/s10973-020-09337-z.
6. Rasool G, Shafiq A, Khan I, Baleanu D, Nisar KS, Shahzadi G. Entropy generation and consequences of MHD in darcy-forchheimer nanofluid flow bounded by non-linearly stretching surface. Symmetry. 2020;12(4):652. doi:10.3390/sym12040652.
7. Tanveer A, Malik MY. Slip and porosity effects on peristalsis of MHD Ree-Eyring nanofluid in curved geometry. Ain Shams Eng J. 2021;12(1):955–68. doi:10.1016/j.asej.2020.04.008.
8. Khan MI, Kadry S, Chu YM, Khan WA, Kumar A. Exploration of Lorentz force on a paraboloid stretched surface in flow of Ree-Eyring nanomaterial. J Mater Res Technol. 2020;9(5):10265–75. doi:10.1016/j.jmrt.2020.07.017.
9. Nadeem S, Khan MN, Abbas N. Transportation of slip effects on nanomaterial micropolar fluid flow over exponentially stretching. Alex Eng J. 2020;59(5):3443–50. doi:10.1016/j.aej.2020.05.024.
10. Waqas H, Imran M, Khan SU, Shehzad SA, Meraj MA. Slip flow of Maxwell viscoelasticity-based micropolar nanoparticles with porous medium: a numerical study. Appl Math Mech. 2019;40(9):1255–68. doi:10.1007/s10483-019-2518-9.
11. Nadeem S, Abbas N, Malik MY. Heat transport in CNTs based nanomaterial flow of non-Newtonian fluid having electro magnetize plate. Alex Eng J. 2020;59(5):3431–42. doi:10.1016/j.aej.2020.05.022.
12. Hayat T, Yaqoob R, Qayyum S, Alsaedi A. Entropy generation optimization in nanofluid flow by variable thicked sheet. Phys A Stat Mech Appl. 2020;551(19):124022. doi:10.1016/j.physa.2019.124022.
13. Alic F. Entransy dissipation analysis and new irreversibility dimension ratio of nanofluid flow through adaptive heating elements. Energies. 2020;13(1):114. doi:10.3390/en13010114.
14. Mkhatshwa MP, Motsa SS, Ayano MS, Sibanda P. MHD mixed convective nanofluid flow about a vertical slender cylinder using overlapping multi-domain spectral collocation approach. Case Stud Therm Eng. 2020;18:100598. doi:10.1016/j.csite.2020.100598.
15. Tlili I, Shahmir N, Ramzan M, Kadry S, Kim JY, Nam Y, et al. A novel model to analyze Darcy Forchheimer nanofluid flow in a permeable medium with Entropy generation analysis. J Taibah Univ Sci. 2020;14(1):916–30. doi:10.1080/16583655.2020.1790171.

16. Khan I, Ullah K, Chu YM, Nisar K, Al-Khaled K. Oldroyd-B nanofluid-flow between stretching disks with thermal slip and multiple flow features. Therm Sci. 2020;24(Suppl 1):83–94. doi:10.2298/tsci20s1083k.
17. Shaw S, Dogonchi AS, Nayak MK, Makinde OD. Impact of entropy generation and nonlinear thermal radiation on darcy-forchheimer flow of $MnFe_2O_4$-casson/water nanofluid due to a rotating disk: application to brain dynamics. Arab J Sci Eng. 2020;45(7):5471–90. doi:10.1007/s13369-020-04453-2.
18. Hayat T, Haider F, Muhammad T, Alsaedi A. On Darcy-Forchheimer flow of carbon nanotubes due to a rotating disk. Int J Heat Mass Transf. 2017;112:248–54. doi:10.1016/j.ijheatmasstransfer.2017.04.123.
19. Muskat M. The flow of homogeneous fluids through porous media. Soil Sci. 1938;46(2):169. doi:10.1097/00010694-193808000-00008.
20. Seddeek MA. Influence of viscous dissipation and thermophoresis on Darcy-Forchheimer mixed convection in a fluid saturated porous media. J Colloid Interface Sci. 2006;293(1):137–42. doi:10.1016/j.jcis.2005.06.039.
21. Francis P, Sambath P, Noeiaghdam S, Fernandez-Gamiz U, Dinarvand S. Computational analysis of bioconvective MHD hybrid nanofluid flow of non-Newtonian fluid over cone/plate:a study based on the Cattaneo-Christov heat and mass flux model. Eng Sci Technol Int J. 2025;63:101970. doi:10.1016/j.jestch.2025.101970.
22. Arulmozhi S, Sukkiramathi K, Santra SS, Edwan R, Fernandez-Gamiz U, Noeiaghdam S. Heat and mass transfer analysis of radiative and chemical reactive effects on MHD nanofluid over an infinite moving vertical plate. Results Eng. 2022;14(1):100394. doi:10.1016/j.rineng.2022.100394.
23. Hayat T, Muhammad T, Al-Mezal S, Liao SJ. Darcy-Forchheimer flow with variable thermal conductivity and Cattaneo-Christov heat flux. Int J Numer Methods Heat Fluid Flow. 2016;26(8):2355–69. doi:10.1108/hff-08-2015-0333.
24. Mohana CM, Kumar BR. Shape effects of Darcy-Forchheimer unsteady three-dimensional CdTe-C/H_2O hybrid nanofluid flow over a stretching sheet with convective heat transfer. Phys Fluids. 2023;35(9):092002. doi:10.1063/5.0168503.
25. Animasaun IL, Kumar TK, Noah FA, Okoya SS, Al-Mdallal QM, Bhatti MM. Insight into Darcy flow of ternary-hybrid nanofluid on horizontal surfaces: exploration of the effects of convective and unsteady acceleration. J Appl Math Mech. 2023;103(5):e202200197. doi:10.1002/zamm.202200197.
26. Prakash J, Tripathi D, Bég OA. Computation of EMHD ternary hybrid non-Newtonian nanofluid over a wedge embedded in a Darcy-Forchheimer porous medium with Zeta potential and wall suction/injection effects. Int J Ambient Energy. 2023;44(1):2155–69. doi:10.1080/01430750.2023.2224339.
27. Das S, Barman B, Jana RN, Makinde OD. Hall and ion slip currents' impact on electromagnetic blood flow conveying hybrid nanoparticles through an endoscope with peristaltic waves. BioNanoScience. 2021;11(3):770–92. doi:10.1007/s12668-021-00873-y.
28. Sahoo A, Nandkeolyar R. Entropy generation and dissipative heat transfer analysis of mixed convective hydromagnetic flow of a Casson nanofluid with thermal radiation and Hall current. Sci Rep. 2021;11(1):3926. doi:10.1038/s41598-021-83124-0.
29. Shaheen N, Ramzan M, Alaoui MK. Impact of Hall current on a 3D Casson nanofluid flow past a rotating deformable disk with variable characteristics. Arab J Sci Eng. 2021;46(12):12653–66. doi:10.1007/s13369-021-06060-1.
30. Rashidi S, Esfahani JA, Maskaniyan M. Applications of magnetohydrodynamics in biological systems—a review on the numerical studies. J Magn Magn Mater. 2017;439(1):358–72. doi:10.1016/j.jmmm.2017.05.014.
31. Basavarajappa M, Bhatta D. Lie group analysis of flow and heat transfer of a nanofluid in cone-disk systems with Hall current and radiative heat flux. Math Methods Appl Sci. 2023;46(14):15838–67. doi:10.1002/mma.9429.
32. Zhang L, Zhang H. Numerical simulation of heat and mass transfer in non-Newtonian Casson nanofluids driven nonlinearly by a wedge-shaped stretching plate. Chin J Phys. 2025;95:939–61. doi:10.1016/j.cjph.2025.04.015.
33. Zhang L, Zhang H, Wang S, Song J, Yao X, Wang W. Boundary layer and entropy analysis of non-Newtonian Casson nanofluids moving nonlinearly in a wedge-shaped stretching plate under an unsteady flow. Case Stud Therm Eng. 2024;56(1):104193. doi:10.1016/j.csite.2024.104193.

34. Khan A, Shah RA, Alam MK, Ahmed H, Shahzad M, Rehman S, et al. Computational investigation of an unsteady non-Newtonian and non-isothermal fluid between coaxial contracting channels: a PCM approach. Results Phys. 2021;28:104570. doi:10.1016/j.rinp.2021.104570.
35. Abbas SZ, Khan WA, Waqas M, Irfan M, Asghar Z. Exploring the features for flow of Oldroyd-B liquid film subjected to rotating disk with homogeneous/heterogeneous processes. Comput Methods Programs Biomed. 2020;189:105323. doi:10.1016/j.cmpb.2020.105323.
36. Sangeetha E, De P. Stagnation point flow of bioconvective MHD nanofluids over Darcy-Forchheimer porous medium with thermal radiation and buoyancy effect. BioNanoScience. 2023;13(3):1022–35. doi:10.1007/s12668-023-01132-y.
37. Gomathi N, Poulomi D. Entropy optimization on EMHD Casson Williamson penta-hybrid nanofluid over porous exponentially vertical cone. Alex Eng J. 2024;108:590–610. doi:10.1016/j.aej.2024.07.092.
38. Shafiq A, Çolak AB, Sindhu TN. Significance of EMHD graphene oxide (GO) water ethylene glycol nanofluid flow in a Darcy-Forchheimer medium by machine learning algorithm. Eur Phys J Plus. 2023;138(3):213. doi:10.1140/epjp/s13360-023-03798-5.
39. Zhao TH, Khan MI, Chu YM. Artificial neural networking (ANN) analysis for heat and entropy generation in flow of non-Newtonian fluid between two rotating disks. Math Methods Appl Sci. 2023;46(3):3012–30. doi:10.1002/mma.7310.
40. Sharma BK, Sharma P, Mishra NK, Fernandez-Gamiz U. Darcy-Forchheimer hybrid nanofluid flow over the rotating *Riga* disk in the presence of chemical reaction: artificial neural network approach. Alex Eng J. 2023;76(1):101–30. doi:10.1016/j.aej.2023.06.014.
41. Boumari E, Amiri MM, Khadang A, Maddah H, Ahmadi MH, Sharifpur M. Numerical investigation of heat transfer in helical tubes modified with aluminum oxide nanofluid and modeling of data obtained by artificial neural network. Numer Heat Transf Part A Appl. 2023;83(3):265–84. doi:10.1080/10407782.2022.2091367.
42. Sundar LS, Mewada HK. Experimental entropy generation, exergy efficiency and thermal performance factor of $CoFe_2O_4$/water nanofluids in a tube predicted with ANFIS and MLP models. Int J Therm Sci. 2023;190:108328. doi:10.1016/j.ijthermalsci.2023.108328.
43. Ouri H, Selimefendigil F, Bouterra M, Omri M, Alshammari BM, Kolsi L. MHD hybrid nanofluid convection and phase change process in an L-shaped vented cavity equipped with an inner rotating cylinder and PCM-packed bed system. Alex Eng J. 2023;63:563–82. doi:10.1016/j.aej.2022.08.016.
44. Beiki H. Developing convective mass transfer of nanofluids in fully developed flow regimes in a circular tube: modeling using fuzzy inference system and ANFIS. Int J Heat Mass Transf. 2021;173:121285. doi:10.1016/j.ijheatmasstransfer.2021.121285.
45. Ahmadi MH, Ghazvini M, Maddah H, Kahani M, Pourfarhang S, Pourfarhang A, et al. Prediction of the pressure drop for CuO/(ethylene glycol-water) nanofluid flows in the car radiator by means of artificial neural networks analysis integrated with genetic algorithm. Phys A Stat Mech Appl. 2020;546:124008. doi:10.1016/j.physa.2019.124008.
46. Hojjat M. Nanofluids as coolant in a shell and tube heat exchanger: ANN modeling and multi-objective optimization. Appl Math Comput. 2020;365:124710. doi:10.1016/j.amc.2019.124710.
47. Shafiq A, Çolak AB, Sindhu TN. Optimization of the numerical treatment of the Darcy-Forchheimer flow of Ree-Eyring fluid with chemical reaction by using artificial neural networks. Int J Numer Methods Fluids. 2023;95(1):176–92. doi:10.1002/fld.5147.
48. Çolak AB, Sindhu TN, Ahmad Lone S, Shafiq A, Abushal TA. Reliability study of generalized Rayleigh distribution based on inverse power law using artificial neural network with Bayesian regularization. Tribol Int. 2023;185:108544. doi:10.1016/j.triboint.2023.108544.
49. Kamsuwan C, Wang X, Seng LP, Xian CK, Piemjaiswang R, Piumsomboon P, et al. Simulation of nanofluid microchannel heat exchanger using computational fluid dynamics integrated with artificial neural network. Energy Rep. 2023;9:239–47. doi:10.1016/j.egyr.2022.10.412.

50. Habib S, Nasir S, Khan Z, Berrouk AS, Islam S, Aamir A. Machine-assisted simulation of heat and mass transfer through a porous Riga surface with chemical reactions and radiation effects. J Therm Anal Calorim. 2025;150(10):7949–70. doi:10.1007/s10973-025-14191-y.
51. Nasir S, Berrouk AS, Gul T. Analysis of chemical reactive nanofluid flow on stretching surface using numerical soft computing approach for thermal enhancement. Eng Appl Comput Fluid Mech. 2024;18(1):2340609. doi:10.1080/19942060.2024.2340609.